THE FMOS-COSMOS SURVEY OF STAR-FORMING GALAXIES AT $z \sim 1.6$. II. THE MASS–METALLICITY RELATION AND THE DEPENDENCE ON STAR FORMATION RATE AND DUST EXTINCTION

H. J. Zahid[1], D. Kashino[2], J. D. Silverman[3], L. J. Kewley[4], E. Daddi[5], A. Renzini[6], G. Rodighiero[7], T. Nagao[8], N. Arimoto[9,10], D. B. Sanders[1], J. Kartaltepe[11], S. J. Lilly[12], C. Maier[13], M. J. Geller[14], P. Capak[15,16], C. M. Carollo[12], J. Chu[1], G. Hasinger[1], O. Ilbert[17], M. Kajisawa[18], A. M. Koekemoer[19], K. Kovač[8], O. Le Fèvre[17], D. Masters[20], H. J. McCracken[21], M. Onodera[12], N. Scoville[22], V. Strazzullo[10], N. Sugiyama[2,4], Y. Taniguchi[18]

and The COSMOS Team

[1] Institute for Astronomy, University of Hawaii at Manoa, Honolulu, HI 96822, USA; jabran@ifa.hawaii.edu
[2] Division of Particle and Astrophysical Science, Graduate School of Science, Nagoya University, Nagoya, 464-8602, Japan
[3] Kavli Institute for the Physics and Mathematics of the Universe (WPI), Todai Institutes for Advanced Study, the University of Tokyo, Kashiwanoha, Kashiwa, 277-8583, Japan
[4] Research School of Astronomy and Astrophysics, The Australian National University, Cotter Road, Weston Creek, ACT 2611, Australia
[5] CEA-Saclay, Service d'Astrophysique, F-91191 Gif-sur-Yvette, France
[6] INAF Osservatorio Astronomico di Padova, vicolo dell'Osservatorio 5, I-35122 Padova, Italy
[7] Dipartimento di Astronomia, Università di Padova, vicolo dell Osservatorio 3, I-35122 Padova, Italy
[8] The Hakubi Center for Advanced Research, Kyoto University, Kyoto 606-8302, Japan
[9] National Astronomical Observatory of Japan, Subaru Telescope, 650 North Aohoku Place, Hilo, HI 96720, USA
[10] The Graduate University for Advanced Studies, Department of Astronomical Sciences, Osawa 2-21-1, Mitaka, Tokyo, 181-8588, Japan
[11] National Optical Astronomy Observatory, 950 N. Cherry Ave., Tucson, AZ 85719, USA
[12] Institute for Astronomy, ETH Zürich, Wolfgang-Pauli-strasse 27, 8093 Zürich, Switzerland
[13] Vienna University, Department of Astrophysics, Tuerkenschanzstrasse 17, 1180 Vienna, Austria
[14] Smithsonian Astrophysical Observatory, 60 Garden Street, Cambridge, MA 02138, USA
[15] California Institute of Technology, 1200 E. California Blvd., Pasadena, CA 91125, USA
[16] Spitzer Science Center, MS 314-6, California Institute of Technology, Pasadena, CA 91125, USA
[17] Aix Marseille Université, CNRS, LAM (Laboratoire d'Astrophysique de Marseille) UMR 7326, 13388, Marseille, France
[18] Research Center for Space and Cosmic Evolution, Ehime University, Bunkyo-cho 2-5, Matsuyama, Ehime 790-8577, Japan
[19] HST and JWST Instruments/Science Division, Space Telescope Science Institute, 3700 San Martin Drive, Baltimore MD 21218, USA
[20] The Observatories of the Carnegie Institution for Science, 813 Santa Barbara Street, Pasadena, CA 91101, USA
[21] Institut d'Astrophysique de Paris, UMR7095 CNRS, Université Pierre et Marie Curie, 98 bis Boulevard Arago, 75014 Paris, France
[22] California Institute of Technology, MC 249-17, 1200 East California Boulevard, Pasadena, CA 91125, USA

ABSTRACT

We investigate the relationships between stellar mass, gas-phase oxygen abundance (metallicity), star formation rate (SFR), and dust content of star-forming galaxies at $z \sim 1.6$ using Subaru/FMOS spectroscopy in the COSMOS field. The mass–metallicity (MZ) relation at $z \sim 1.6$ is steeper than the relation observed in the local universe. The steeper MZ relation at $z \sim 1.6$ is mainly due to evolution in the stellar mass where the MZ relation begins to turnover and flatten. This turnover mass is 1.2 dex larger at $z \sim 1.6$. The most massive galaxies at $z \sim 1.6$ ($\sim 10^{11}\ M_\odot$) are enriched to the level observed in massive galaxies in the local universe. The MZ relation we measure at $z \sim 1.6$ supports the suggestion of an empirical upper metallicity limit that does not significantly evolve with redshift. We find an *anti*-correlation between metallicity and SFR for galaxies at a fixed stellar mass at $z \sim 1.6$, which is similar to trends observed in the local universe. We do not find a relation between stellar mass, metallicity, and SFR that is independent of redshift; rather, our data suggest that there is redshift evolution in this relation. We examine the relation between stellar mass, metallicity, and dust extinction, and find that at a fixed stellar mass, dustier galaxies tend to be more metal rich. From examination of the stellar masses, metallicities, SFRs, and dust extinctions, we conclude that stellar mass is most closely related to dust extinction.

Key words: galaxies: abundances – galaxies: evolution – galaxies: fundamental parameters – galaxies: ISM

Online-only material: color figures

1. INTRODUCTION

Near-infrared multi-object spectrographs placed on 8–10 m class telescopes have recently opened up the redshift desert ($1 < z < 2$) for spectroscopic exploration. This redshift range is particularly important since it marks the epoch where galaxies transition from the peak of cosmic star formation to the more quiescent build-up of stellar mass that we see in galaxies today (Hopkins & Beacom 2006, and references therein). Understanding of the physical processes responsible for this transition is crucial for building a coherent picture of galaxy evolution. In this series of papers, we report on the first results of our recent survey of star-forming galaxies at

$1.4 < z < 1.7$. We present the sample and survey design in J. Silverman et al. (in preparation, hereafter Paper III) and the spectroscopically measured, extinction-corrected star formation rates (SFRs) in Kashino et al. (2013, hereafter Paper I). Here, we present on the relation between stellar mass, gas-phase oxygen abundance, SFR, and dust extinction for our sample.

The gas-phase oxygen abundance (metallicity) is a crucial diagnostic of galaxy evolution. Oxygen is the most abundant heavy element produced in massive stars and comprises half the mass of heavy elements in the universe. Therefore, the abundance of oxygen is an excellent proxy of chemical evolution. Oxygen is dispersed into the interstellar medium (ISM) of galaxies by massive stars through stellar winds and supernovae.

The mass of oxygen in the ISM accumulates as galaxies build-up stellar mass. However, metallicity is a measure of the amount of oxygen *relative* to hydrogen. Therefore, it is not simply an accumulated record of star formation, but also a sensitive tracer of gas flows. The inflow of pristine gas can dilute the abundance of oxygen and decrease the metallicity, but inflows also fuel star formation, leading to the synthesis of heavy elements. At the same time, feedback from massive stars is one of the primary mechanisms by which gas is expelled from galaxies (e.g., Mathews & Baker 1971; Larson 1974). It is clear that outflows can transport metals out of galaxies (Renzini 1997; Martin et al. 2002; Kirby et al. 2011; Bordoloi et al. 2011; Newman et al. 2012; Zahid et al. 2012b). However, the impact that outflows have on metallicity remains uncertain since the composition of outflowing material is not well constrained observationally.

Using observations of eight local star-forming galaxies, Lequeux et al. (1979) first showed that metallicity increases with stellar mass. In subsequent years, samples have grown considerably. Tremonti et al. (2004) establish a tight (∼0.1 dex scatter) mass–metallicity (MZ) relation in the local universe by examining ∼50,000 galaxies from the Sloan Digital Sky Survey (SDSS) with stellar masses ranging from $10^{8.5} \gtrsim M_*/M_\odot \gtrsim 10^{11}$. The relation has since been extended down to $\sim10^6\,M_\odot$ (Lee et al. 2006; Zahid et al. 2012a; Berg et al. 2012). Surveys of distant galaxies have made it possible to study the MZ relation at intermediate (Savaglio et al. 2005; Maier et al. 2005; Zahid et al. 2011, 2013a; Pérez-Montero et al. 2013) and high redshifts (Erb et al. 2006; Maiolino et al. 2008; Mannucci et al. 2009; Laskar et al. 2011; Yabe et al. 2012; Yuan et al. 2013; Kulas et al. 2013). At a fixed stellar mass, galaxies are less enriched at higher redshifts. While the origin of this relation is still debated, measurements of the chemical evolution of galaxies provide important constraints for the processes of star formation and gas flows in models of galaxy evolution (e.g., Brooks et al. 2007; Finlator & Davé 2008; Davé et al. 2011; Zahid et al. 2012b, 2014; Torrey et al. 2013; Lilly et al. 2013).

While almost all studies conclude that the gas in galaxies becomes more metal-rich as the universe evolves, some studies also report a flattening of the MZ relation for massive galaxies at late times (Savaglio et al. 2005; Maier et al. 2005; Maiolino et al. 2008; Zahid et al. 2011, 2013a). Many of these works (Savaglio et al. 2005; Maier et al. 2006; Maiolino et al. 2008; Zahid et al. 2011) attribute this flattening to galaxy downsizing (Cowie et al. 1996), i.e., the process by which star formation becomes more dominant in lower mass systems at late times. However, we show that flattening of the slope of the MZ relation is more consistent with the process of metallicity saturation rather than strictly a consequence of downsizing (Zahid et al. 2013a). In this study, we revisit this issue and extend our analysis to $z \sim 1.6$.

In the local universe, the metallicity at a fixed stellar mass appears to be correlated with SFR (Ellison et al. 2008; Lara-López et al. 2010; Mannucci et al. 2010; Yates et al. 2012; Andrews & Martini 2013). Mannucci et al. (2010) suggest that the relation between stellar mass, metallicity, and SFR that minimizes the scatter for local galaxies does not evolve out to $z \sim 2.5$. However, several studies have shown that this relation is dependent on methodology (Yates et al. 2012; Andrews & Martini 2013). We examine the relation between stellar mass, metallicity, and SFR at $z \sim 1.6$, applying a consistent methodology throughout.

The paper is organized as follows. In Sections 2 and 3, we describe our data and methodology, respectively. In Section 4, we examine emission line diagnostics using a subset of our sample where we have both *J*- and *H*-band observations. In Section 5, we present the main results of our study and we discuss potential systematic issues in our measurements in Section 6. In Section 7, we discuss our results and we present a summary in Section 8. When necessary, we adopt a standard cosmology with $(H_0, \Omega_m, \Omega_\Lambda) = (70\ \mathrm{km\ s^{-1}\ Mpc^{-1}}, 0.3, 0.7)$ and a Chabrier (2003) initial mass function (IMF).

2. DATA

2.1. FMOS-COSMOS Observations

Details of the survey design and observations are presented in Paper III. Here, we summarize the most relevant aspects. We emphasize that, when necessary, measured quantities are converted from the Salpeter (1955) IMF used in Papers I and III to the Chabrier (2003) IMF used in this work. This is done for consistency with our previous metallicity studies.

Our observations are carried out using the near-infrared Fiber Multi-Object Spectrograph (FMOS; Kimura et al. 2010) on the Subaru Telescope. FMOS has 400 1″.2 fibers distributed over a 30′ diameter circular field of view. We operate the spectrograph in cross-beam switching mode. Two fibers are allocated to each object. The spectrograph dithers between two positions such that one of the two fibers is always on source while the other fiber is used for sky subtraction. This procedure allows us to observe ∼200 galaxies with simultaneous sky observations for optimal sky subtraction. An OH-airglow suppression filter blocks the strongest atmospheric emission lines (Iwamuro et al. 2001). Our observations are taken using the high-resolution mode, which has a spectral resolution of $R \sim 2200$. At this resolution, the [N II]λ6584 and Hα lines are well-resolved in star-forming galaxies (see Figure 1 in Kashino et al. 2013) and contamination from narrow sky lines is minimized. For galaxies at $1.4 < z < 1.7$, we can observe Hα and Hβ in the *H*-long (1.60–1.80 μm) and *J*-long (1.11–1.35 μm) bands, respectively.

We primarily target star-forming galaxies in the redshift range of $1.4 < z < 1.7$ in the central square degree of the COSMOS field (Scoville et al. 2007). We preselect galaxies using robust photometric redshifts from the catalog of Ilbert et al. (2009). These redshifts are based on 30 bands of photometry ranging from the UV to the mid-infrared. In order to efficiently target star-forming galaxies, we require K_s-band magnitudes < 23. For the majority of the sample, we use an sBzK selection (Daddi et al. 2004) using the catalog of McCracken et al. (2010). A significant number of objects, however, were selected based on stellar mass and photo-z (see Paper III). To minimize AGN contamination, we exclude galaxies that have X-ray detections. We revisit this issue in Sections 4 and 6.

The *H*-band observations of 796 galaxies were carried out over six nights in 2012 March and two nights in 2013 January. Each galaxy was observed for approximately five hours allowing us to reach a 3σ flux limit of 4×10^{-17} erg s^{-1} cm^{-2} corresponding to an unobscured SFR limit of $\sim5\,M_\odot$ yr^{-1}. A subsample of galaxies with Hα detections satisfying a signal-to-noise ratio (S/N) > 3 were observed in the *J* band in order to obtain measurements of Hβ and [O III]λ5007. These observations were carried out in 2012 March, 2012 December, and 2013 February with an on-source integration time of approximately five hours.

All data were reduced with the FMOS Image-Based Reduction Package (Fibre-pac; Iwamuro et al. 2012). In cross-beam switching mode, the sky is observed simultaneously along with
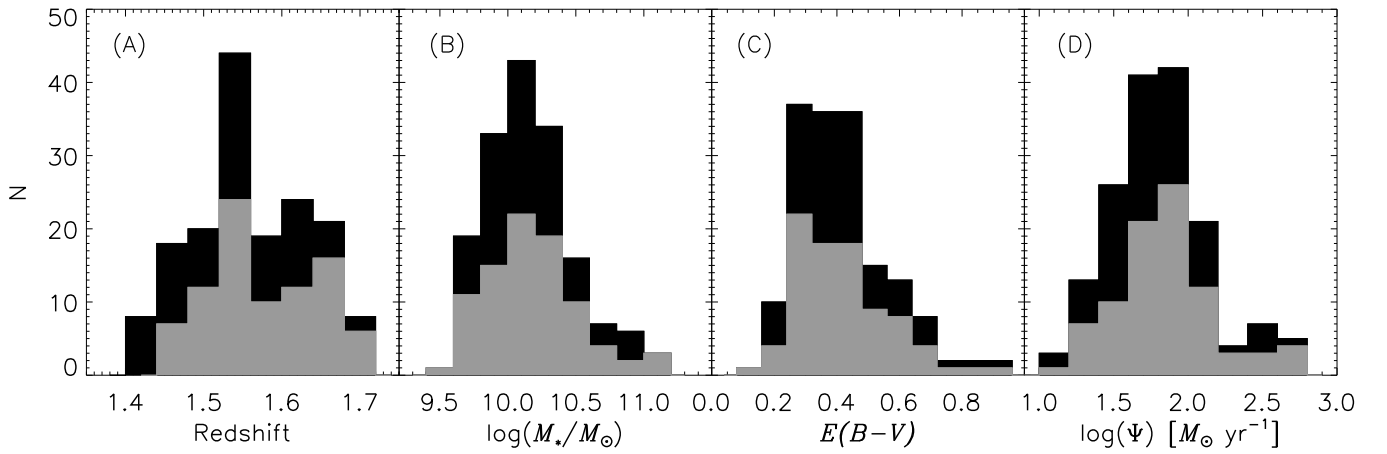
Figure 1. (A) Redshift, (B) stellar mass, (C) nebular $E(B - V)$, and (D) SFR distribution of our sample of galaxies at $z \sim 1.6$. The black histogram shows the distribution for our sample of 162 Hα detected galaxies. The gray histogram shows the distribution for the subsample of 85 Hα detected galaxies that are observed both in the J- and H-bands.

the target. Initial sky subtraction is performed by differencing the fiber pair. Next, the detector cross-talk and bias difference between the quadrants are corrected and the flat fielding is performed. After the bad pixels are rejected, the image is corrected for distortion and the residual sky is subtracted. The images from multiple exposures are combined to produce a single spectrum per object. The wavelength is calibrated based on the Th-Ar spectral images taken just before the science exposure with a typical accuracy of >1 pixel ($\sim$1 Å in high-resolution mode). The flux calibration is carried out using flux standard stars that are observed simultaneously with other scientific targets.

From our observations, we selected 168 galaxies with significant Hα detections (S/N > 3). A subsample of 89 galaxies also have corresponding J-band observations. For the metallicity analysis, we remove galaxies whose Hα emission is near the edge of the detector and therefore [N II]λ6584 is not observed. Our final sample consists of 162 star-forming galaxies observed in the H band with significant (S/N > 3) detections of Hα emission and a subsample of 87 galaxies with corresponding J-band observations. The measured physical properties of both samples are shown in Figure 1. Figure 1 shows that the subsample of galaxies for which we have J-band observations is representative of the larger H-band sample.

2.2. The Local Sample

We derive the local MZ relation using data from the SDSS Legacy Survey (SDSS I–II). The latest release of the Legacy data is found in the DR8 (Aihara et al. 2011). The spectroscopic data consists of $\sim$900,000 galaxies spanning a redshift range of $0 < z < 0.7$. The survey has a limiting magnitude of $r = 17.8$ and covers 8000 deg^2 on the sky (Strauss et al. 2002). The nominal spectral range of the observations is 3800–9200 Å with a spectral resolution of $R = 1800$–2000. We use the most recent $ugriz$-band c-model magnitudes released as part of the DR8 (Padmanabhan et al. 2008). We use the latest emission line flux measurements released by the Portsmouth Group[23] (Thomas et al. 2013). The line fluxes are corrected for dust extinction using the correction equation from Calzetti et al. (2000) and only the corrected fluxes are given in the catalog. In order to derive dust extinction from the Balmer decrement, we use the

MPA/JHU group catalog[24] of line flux measurements, which are not corrected for dust extinction.

We select galaxies in a limited redshift range with $z < 0.12$ to minimize evolutionary effects and we require an aperture covering fraction $\gtrsim$20% to avoid biasing our metallicity estimate (Kewley et al. 2005). Ellison et al. (2008) show that metallicities are correlated to galaxy size and therefore aperture effects may bias the MZ relation. However, the MZ relation we derive does not strongly depend on the minimum covering fraction we apply in selecting the sample. This could result from the fact that massive galaxies, which are most affected by aperture effects, tend to have shallow metallicity gradients. Integral field surveys of local galaxies currently underway will definitely address systematic biases related to covering fractions.

Our primary selection criteria for galaxies are the S/Ns of strong emission lines. The results presented in this paper are based on analysis of the Hβ, [O III]λ5007, Hα, and [N II]λ6584 emission lines. Foster et al. (2012) show that the MZ relation is insensitive to the S/N threshold adopted for the Hβ, Hα, and [N II]λ6584 emission lines. However, they also show that S/N cuts on the [O III]λ5007 line can lead to a significant bias in the MZ relation. We require an S/N > 3 in the Hβ, Hα, and [N II]λ6584 emission lines but make no S/N cut on the [O III]λ5007 line.

Metallicities are determined from line flux ratios under the assumption that massive stars produce the EUV radiation field that ionized the nebular gas. Therefore, metallicities determined in galaxies where active galactic nuclei (AGNs) significantly contribute to the ionizing radiation are not reliable. AGNs are removed from the sample using the [O III]/Hβ versus [N II]/Hα line flux ratio diagram (i.e., the BPT method, Baldwin et al. 1981; Kauffmann et al. 2003; Kewley et al. 2006). Star-forming galaxies are well-separated from AGNs in the [O III]/Hβ versus [N II]/Hα line flux ratio diagram and here we apply the separation given in Kewley et al. (2006) to remove AGNs. Galaxies with

$$\log([\text{O III}]/\text{H}\beta) < 0.61/[\log([\text{N II}]/\text{H}\alpha) - 0.05] + 1.3 \quad (1)$$

are defined as star-forming. Here, [O III], Hβ, [N II], and Hα are the emission line strengths of [O III]λ5007, Hβ, [N II]λ6584, and Hα, respectively.

Our final sample consists of ∼88,000 star-forming galaxies in the redshift range of $0.02 < z < 0.12$.

3. METHODS

3.1. Metallicity Determination

Collisionally excited emission lines are the primary coolants in H II regions. Their line strengths scale with temperatures and metallicity. Therefore, flux ratios of collisionally excited emission lines to recombination emission lines can be used to estimate metallicity. Various ratios have been calibrated either empirically or theoretically to yield estimates of the gas-phase oxygen abundance. Different calibrations applied to the same galaxies can give metallicities that range up to ∼0.6 dex (Kewley & Ellison 2008). Thus, there is great uncertainty in the absolute metallicity scale with empirically calibrated diagnostics typically yielding metallicities that are ∼0.3 dex smaller than theoretically calibrated diagnostics. It is beyond the scope of this paper to discuss the details of various diagnostics and possible resolutions. We refer the reader to detailed discussions of this issue presented in Kewley & Ellison (2008). However, we note that despite the uncertainty in absolute metallicities, Kewley & Ellison (2008) find that relative metallicities determined using various diagnostics are robust. This is fortunate since we are able to apply the same method for determining metallicity in both our local sample from SDSS and our sample of galaxies at $z \sim 1.6$.

We determine metallicities using the commonly used $N2$ diagnostic calibrated by Pettini & Pagel (2004, PP04 hereafter). Here, $N2$ is defined as the log of the emission line ratio between [N II]$\lambda6584$ and Hα. The advantage of this ratio is that the lines are closely spaced in wavelength and therefore can be easily observed simultaneously in the H band for galaxies at $1.4 < z < 1.7$. Additionally, because we are taking a flux ratio and the lines are only separated by ∼20 Å, no extinction correction is required. PP04 calibrate the line ratio using a semi-empirical approach. At lower metallicities, they empirically determine metallicities from temperature sensitive auroral lines. This method is known as the "direct" method and it provides a well-established metallicity scale below solar metallicities. However, the [O III]$\lambda4363$ auroral line used in determining metallicities with the "direct" method is extremely weak. Because the line strength decreases exponentially with increasing metallicity, it is not observed in metal-rich H II regions. PP04 use photoionization modeling of individual H II regions to calibrated metallicities in metal-rich regions where the direct method cannot be applied. We apply the linear calibration given by

$$12 + \log(O/H) = 8.90 + 0.57 \times N2. \quad (2)$$

The calibration is valid for $-2.5 < N2 < -0.3$. The formal statistical errors of the slope and intercept are 0.03 and 0.04, respectively, and the intrinsic dispersion is 0.18 dex. We note that PP04 also provide a quadratic calibration of the N2 ratio. While the quadratic calibration gives a quantitatively different MZ relation, the major conclusions of this work rely on the relative accuracy of the diagnostics and are independent of the particular calibration. Throughout this work, we provide the measured N2 values along with the inferred metallicities.

PP04 also calibrate the $O3N2$ line ratio, which is defined as $\log\{([O III]/H\beta)/([N II]/H\alpha)\}$. Here, [O III] refers to the line flux of [O III]$\lambda5007$, and [N II] refers to the line flux of [N II]$\lambda6584$. The metallicity calibration for this ratio is

$$12 + \log(O/H) = 8.73 - 0.32 \times O3N2. \quad (3)$$

Because the $N2$ and $O3N2$ line ratios are calibrated using the same data, they should be consistent. However, several studies of high-redshift galaxies have reported systematic differences in the metallicities determined using this ratio (e.g., Erb et al. 2006; Yabe et al. 2012). Since we measure the [O III] and Hβ lines in a subset of our galaxies, we are able to asses the consistency of these two ratios at $z \sim 1.6$ (see Section 4.2).

Several authors have independently calibrated the $N2$ ratio (Denicoló et al. 2002; Nagao et al. 2006; Marino et al. 2013). While the calibrations vary systematically, they are all consistent with a monotonically increasing, quasi-linear relation between metallicity and $N2$. We emphasize that while the absolute metallicity is uncertain and varies systematically depending on the calibration applied, the relative metallicities determined from $N2$ are robust over the range of metallicities explored in this study. The results and conclusions of this study rely on the relative metallicities being accurate. In Table 1, we provide the measured $N2$ ratio and the metallicities derived using the PP04 calibration.

3.2. Mass Determination

For the SDSS sample, we determine the stellar masses from the *ugriz*-band photometry (Stoughton et al. 2002). The stellar masses for the FMOS sample are determined from 30 band UV to IR photometry (Capak et al. 2007).

We use the Le Phare[25] code developed by S. Arnouts & O. Ilbert to estimate stellar masses. We estimate the stellar masses of galaxies by comparing photometry with stellar population synthesis models in order to determine the mass-to-light (M/L) ratio. The M/L ratio is then used to scale the observed luminosity (Bell et al. 2003; Fontana et al. 2004). Magnitudes are synthesized from the stellar templates of Bruzual & Charlot (2003) and we use a Chabrier (2003) IMF. The 27 models have two metallicities and seven exponentially decreasing star formation models (SFR $\propto e^{-t/\tau}$) with $\tau = 0.1, 0.3, 1, 2, 3, 5, 10, 15$, and 30 Gyr. We apply the extinction law of Calzetti et al. (2000) allowing $E(B - V)$ to range from 0 to 0.6 and the stellar population ages range from 0 to 13 Gyr. Conroy et al. (2009) estimate that systematic errors in stellar mass are ∼0.3 dex for local galaxies. We have applied a consistent procedure for measuring the stellar masses for our different samples in order to mitigate systematic uncertainties and derive a relatively robust estimate.

We use the Kennicutt (1998) relation between the synthesized UV luminosity and SFR to correct for the emission line contributions to the photometry. This treatment accounts for Hα, Hβ and [O II]$\lambda3727$, and [O III]$\lambda4959, 5007$ (Ilbert et al. 2009). We have determined stellar masses using broadband photometry and therefore the emission line corrections are small. In Zahid et al. (2011), we compare this method with the method used by the MPA/JHU group to determine stellar masses of the SDSS galaxies. We find that the dispersion between the two methods is 0.14 dex, which is consistent with the observational uncertainties. The stellar mass distribution of our sample is plotted in Figure 1(B).

3.3. $E(B - V)$ Determination

For the local sample, we measure dust extinction from the Balmer decrement. For case B recombination with electron

---

[25] http://www.cfht.hawaii.edu/∼arnouts/LEPHARE/cfht_lephare/lephare.html

Table 1
FMOS-COSMOS MZ Relation Data

Stellar Mass	N2	12+log(O/H)	log(Ψ)	E(B − V)	N
log($M_*/M_\odot$)	log([N II]/Hα)	PP04	($M_\odot$ yr^{-1})	Nebular	
9.70	−0.951 ± 0.066	8.358 ± 0.038	1.175 ± 0.048	0.267 ± 0.012	16
9.83	−0.909 ± 0.060	8.382 ± 0.034	1.258 ± 0.059	0.279 ± 0.021	16
9.95	−0.783 ± 0.038	8.454 ± 0.022	1.397 ± 0.051	0.342 ± 0.020	16
10.05	−0.733 ± 0.038	8.482 ± 0.021	1.415 ± 0.056	0.357 ± 0.024	16
10.11	−0.678 ± 0.043	8.514 ± 0.024	1.509 ± 0.046	0.351 ± 0.034	16
10.17	−0.676 ± 0.034	8.515 ± 0.019	1.512 ± 0.076	0.403 ± 0.030	16
10.25	−0.647 ± 0.033	8.531 ± 0.019	1.702 ± 0.044	0.442 ± 0.032	15
10.35	−0.548 ± 0.024	8.587 ± 0.014	1.699 ± 0.054	0.466 ± 0.019	15
10.50	−0.435 ± 0.022	8.652 ± 0.013	1.824 ± 0.057	0.525 ± 0.037	15
10.83	−0.419 ± 0.023	8.661 ± 0.013	2.206 ± 0.093	0.679 ± 0.044	15

Notes. Column 1 gives the median stellar mass for each of the ten mass bins. Columns 2 and 3 are the fitted $N2$ ratio and corresponding 12+log(O/H) using the PP04 calibration, respectively. The errors only represent the observational uncertainties and do not include the 0.18 dex intrinsic dispersion of the metallicity calibration. Columns 4 and 5 are the median SFR and median $E(B − V)$ in each bin, respectively. The number of spectra averaged in each bin, N, is given in Column 6.

temperature $T_e = 10^4$ K and electron density $n_e = 10^2$ cm^{-3}, the intrinsic Hα/Hβ ratio is expected to be 2.86 (Hummer & Storey 1987). We obtain the intrinsic color excess, $E(B − V)$ using the extinction curve of Calzetti et al. (2000). Groves et al. (2012) suggest that Hβ equivalent widths and line fluxes provided in the SDSS DR7 are underestimated due to improper correction for Hβ absorption. We apply the correction they recommend. The typical correction is small, reducing the $E(B − V)$ by ∼0.03.

We detect Hβ in very few individual galaxies at $z ∼$ 1.6. Therefore, we are not able to measure extinction from the Balmer decrement in individual galaxies. In Paper I, we determine stellar reddening, $E_{star}(B − V)$, from the observed $B_J − z$ color (Daddi et al. 2007). We average our FMOS-COSMOS spectra in three bins of $E_{star}(B − V)$. We measure the Hβ and Hα line fluxes and derive the Balmer decrement and nebular reddening, $E_{neb}(B − V)$, from these average spectra. We determine the average factor $f = 0.76$, which relates stellar reddening to nebular reddening, i.e., $E_{neb}(B − V) = E_{star}(B − V)/f$. We convert the stellar reddening determined from the observed $B_J − z$ color of individual galaxies into a nebular reddening, $E_{neb}(B − V)$, using our correction factor, f. The extinction correction, $A_{Hα}$, ranges between 0.6 ∼ 1.7. Hereafter, all references to $E(B − V)$ are to $E_{neb}(B − V)$, derived from the stellar extinction using the $f = 0.76$ factor. The $E(B − V)$ distribution is plotted in Figure 1(C).

3.4. SFR Determination

For the SDSS sample, Brinchmann et al. (2004) measure SFRs from the Balmer lines, but apply an aperture correction based on the galaxy colors measured inside and outside the fiber. Salim et al. (2007) improve this correction by comparing SFRs determined from Balmer lines with SFRs determined from UV photometry. We emphasize that aperture corrections to the SFR are important since the 3″ SDSS fibers typically cover less than half of the galaxy light (Kewley et al. 2005; Zahid et al. 2013c). The aperture-corrected SFRs are made available by the MPA/JHU group in the DR7 and we adopt them in this work. We convert the SFRs to a Chabrier IMF by subtracting 0.05 dex from the DR7 measurements.

We measure SFRs for galaxies at $z ∼$ 1.6 from extinction-corrected Hα luminosities using the calibration from Kennicutt (1998). The measurements in Paper I are based on the Salpeter

(1955) IMF. We scale down these measurements by a factor of 1.7 for consistency with the Chabrier (2003) IMF we use in this work. The cosmology adopted in Paper I is $\Omega_m = 0.25$ and $\Omega_\Lambda = 0.75$. This differs from the cosmology adopted in this work ($\Omega_m = 0.3$, $\Omega_\Lambda = 0.7$). We scale the SFRs used in this work down by a factor of 0.035 dex to convert between the two cosmologies. The FMOS fibers are 1″2 and therefore do not typically fully cover most galaxies at $z ∼$ 1.6 under typical seeing conditions. We correct for fiber losses by applying an aperture correction to the data. The aperture correction is derived by convolving *Hubble Space Telescope*/ Advanced Camera for Surveys *I*-band images with the seeing conditions of our observation and extracting 1″2 aperture flux and comparing it to total flux. This procedure assumes that the Hα and UV emission have the same spatial distribution. The Hα flux is scaled by the aperture correction factor, which ranges between 1.2 ∼ 5 with a typical value of ∼2.

The SFR distribution of our sample is shown in Figure 1(D).

3.5. Averaging Spectra

In star-forming galaxies, the [N II] emission line is significantly weaker than Hα. Because the line scales with metallicity, it is more likely to be detected in metal-rich galaxies and is detected in only a small fraction of our sample. In order to derive an unbiased MZ relation, we rely on stacking multiple spectra sorted by stellar mass in order to measure an average [N II]/Hα ratio. We find that [N II] can be measured with reasonable S/N in even the least massive (lowest metallicity) galaxies in our sample by stacking ∼16 spectra.

We tried various methods for stacking the data including error-weighted averages, medians, and stacking of spectra normalized to luminosity or SFR. In each case, the MZ relation we derive was statistically consistent. We adopt the procedure described below because it yields the smallest χ^2 fit of the MZ relation.

We sort galaxies into bins of stellar mass and average the spectra. We convert the observed frame flux vector of each observation to the rest-frame flux vector using the measured redshift. We then interpolate the flux and error spectrum of each galaxy using a 0.5 Å per pixel sampling. This wavelength sampling corresponds to the observed frame single pixel resolution of FMOS (1.25 Å) for galaxies at $z = 1.5$. Before averaging over the multiple observations, we perform two cuts. First, we
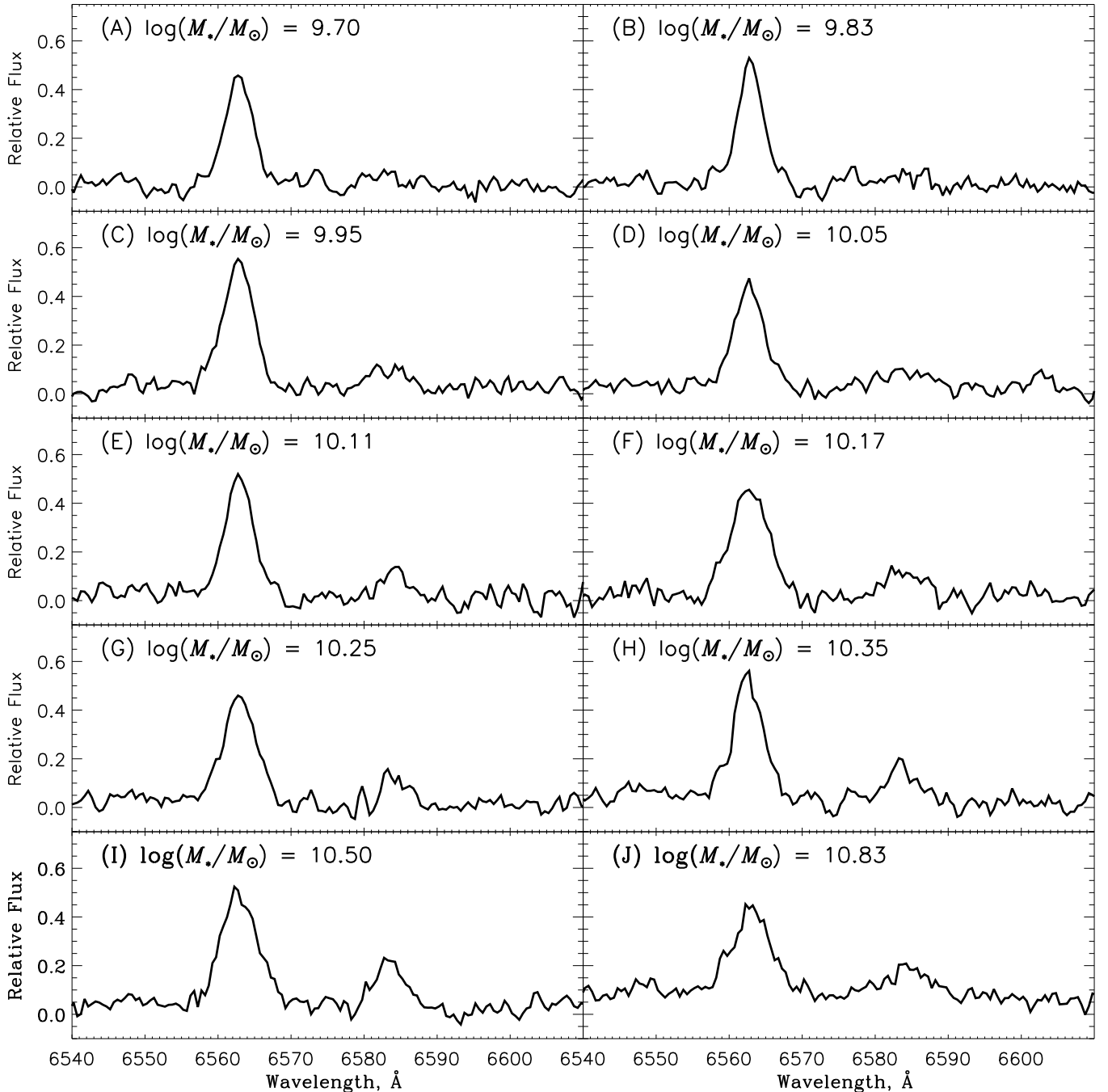
Figure 2. FMOS spectra sorted and averaged in 10 stellar mass bins. The median stellar mass of each bin is listed in each panel.

remove pixels in regions contaminated by strong residual sky lines. These regions are easily identified in the error spectrum by their relatively large errors. This cut typically removes ∼10% of the data in each resampled pixel bin. Second, we calculate a resistant mean using the *resistant_mean.pro* routine in IDL, which is part of the robust statistics package in the Astronomy Users Library. We clip all of the data that are five median absolute deviations from the median of the distribution of each pixel. This procedure typically cuts out ∼2% of the data. Our results are not sensitive to the specific level adopted for the two cuts. The error of each resolution element in the average is determined from the observational uncertainties of the individual pixels in each spectra added in quadrature. Figure 2 shows the stacked spectra.

A serious concern is that the data cuts we have applied may bias the MZ relation we derive in Section 5.1. In order to assess the impact of our cuts on the MZ relation, we apply each of the cuts described above in turn. The MZ relation we derive by averaging the data without applying any cuts is statistically consistent with the relation we derive with the cuts applied. When no cuts are applied, the average error in the metallicity we measure from the average spectra is $\bar{\sigma} = 0.11$ dex, and the χ^2 of the fit to the MZ relation is 2.9. By removing ∼10% of the data in regions contaminated by strong sky lines, we reduce the average error in the metallicity to $\bar{\sigma} = 0.036$ dex and derive an improved fit with $\chi^2 = 2.4$. Finally, by using the resistant mean and removing ∼2% of the data, the average errors remain the same, but the derived fit is improved to $\chi^2 = 1.6$.
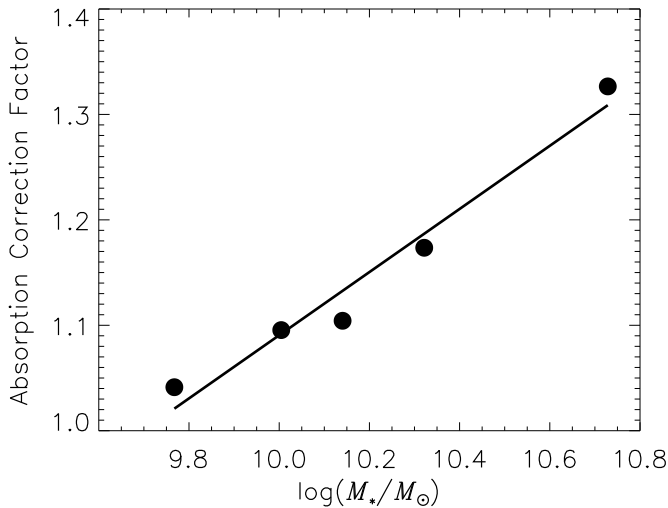
Figure 3. Factor by which the Hβ line-flux-corrected for Balmer absorption is greater than the Hβ line flux without an absorption correction. The factor is determined from average galaxy spectra sorted in five bins of stellar mass.

We conclude that the procedure we apply in removing data does not bias our derived relation, but does significantly reduce the errors in metallicity and improve the fit of the MZ relation.

3.6. Line Fitting

We fit emission lines using the *MPFIT* package of routines implemented in IDL (Markwardt 2009). The [N II]λ6584 and Hα lines are simultaneously fit with a Gaussian profile. We first subtract away the continuum by fitting a line to the pixels in 40 Å windows on either side of the emission lines. We then perform a χ^2 minimization to fit the width, amplitude, and central wavelength of each emission line. The line widths of the [N II]λ6584 and Hα emission lines are forced to be the same. We adopt the area of the Gaussian determined from the fit parameters as our estimate of the line flux, and we propagate the observational uncertainties to the fit parameters and flux estimates.

For a subset of our galaxies, we have *J*-band observations of the [O III]λ5007 and Hβ emission lines. We follow an identical procedure for estimating line fluxes for these lines as we do for [N II] and Hα, but with one notable exception. Balmer absorption arising in the atmospheres of intermediate-mass A-type stars can lead to underestimates of the Hβ emission line flux. This is because the emission line sits in an absorption trough which leads to a flux decrement (e.g., see Figure 3 in Zahid et al. 2011). We correct for this underlying absorption by fitting the continuum using stellar population synthesis models. Here, we combine our *J*-band and *H*-band observations. We average our 87 spectra in 5 stellar mass bins. We mask out emission lines and fit the continuum in the average spectra with a linear combination of Bruzual & Charlot (2003) models convolved to the FMOS instrument resolution.

Figure 3 shows the Balmer absorption correction factor derived by comparing the fluxes measured with and without an absorption correction. The absorption correction factor is defined as $F(H\beta)_{corr}/F(H\beta)$. Here, $F(H\beta)_{corr}$ and $F(H\beta)$ are the Hβ line fluxes measured from our stacked data with and without an absorption correction, respectively. The linear fit is given by

$$F(H\beta)_{corr}/F(H\beta) = 1.09 + 0.30[\log(M_*/M_\odot) - 10]. \quad (4)$$

The Hβ emission line Balmer absorption correction ranges from $1 \sim 1.5$ for galaxies in our sample with a median of 1.27. For the BPT analysis in the following section, we apply the absorption correction given by Equation (4) to individual galaxies. The absorption correction for Hα is small ($\lesssim 2\%$; see Paper I). Thus, we make no correction for Hα absorption.

We derive the formal errors by propagating the observational uncertainties of each pixel through to the fit parameters from which we determine line fluxes. These errors are then propagated to the line ratios and metallicities in the standard way. The formal errors only reflect the quality of the data and do not account for the intrinsic scatter in the line flux ratios due to the intrinsic scatter in the MZ relation (Zahid et al. 2012a). Within each stellar mass bin, we estimate the intrinsic scatter in the metallicities by bootstrapping the data. In each bin of stellar mass, we randomly select, with replacement, N spectra and average using the procedure described above. Here, N is the number of spectra in each bin of stellar mass (see Table 1). We perform this procedure 1000 times for each of the mass bins, determining the line fluxes and metallicities from the average spectra each time. Given the small number of spectra in each mass bin ($\sim$16), it is unlikely that we are sampling the full scatter in line fluxes and metallicities. The scatter derived using the bootstrap is therefore a lower limit to the intrinsic scatter.

4. EMISSION LINE DIAGNOSTICS

4.1. AGN Contamination

The [O III]/Hβ versus [N II]/Hα diagnostic diagram is commonly used to classify galaxies as star-forming or active galactic nuclei (AGN Baldwin et al. 1981; Kauffmann et al. 2003; Kewley et al. 2006). The line flux of [O III]λ5007 relative to Hβ is plotted against the line flux of [N II]λ6584 relative to Hα. Recently, Kewley et al. (2013a) suggested that the physical conditions of the ISM and radiation field evolve with redshift, thus leading to a cosmic evolution of the locus of star-forming and AGN galaxies on the [O III]/Hβ versus [N II]/Hα diagnostic diagram. By comparing their theoretical models to observations, Kewley et al. (2013b) derived a redshift-dependent classification given by

$$\log([O\,III]/H\beta) = \frac{0.61}{\log([N\,II]/H\alpha) - 0.02 - 0.1833z} + 1.2 + 0.03z. \quad (5)$$

Galaxies below and above the dividing line defined by Equation (5) are classified as star-forming and AGNs, respectively.

In Figure 4, we plot the [O III]/Hβ versus [N II]/Hα line ratios for 72 individual galaxies with Hα and [O III]λ5007 detections. We also plot the ratios for average spectra of 87 galaxies sorted into five mass bins. The emission line properties are determined from averaging 16 or 17 spectra in each stellar mass bin. The blue error bars are the formal observational uncertainties and the red error bars are the bootstrapped errors, which estimate the intrinsic scatter of the data. The red dashed and blue solid curves are the local and $z \sim 1.6$ classifications determined from Equation (5), respectively. We find that our sample of galaxies have an excitation that is nearly consistent with the locus of local star-forming galaxies (compare to contours and the red-dashed line). Comparison with the $z \sim 1.6$ classification line reveals that most of our galaxies lie well within the star-forming sequence. The six galaxies denoted by stars are identified as
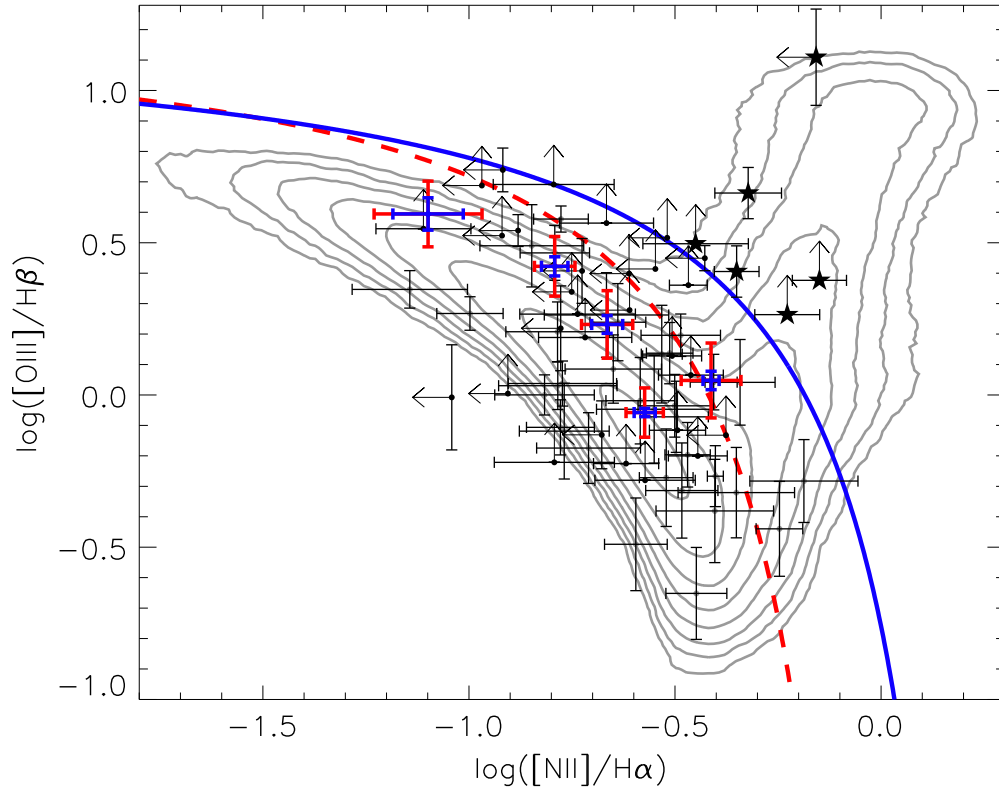
Figure 4. [O III]/Hβ vs. [N II]/Hα diagram for the subsample of our galaxies with both *J*- and *H*-band observations. Individual galaxies are shown in black. The objects denoted by stars are identified as AGNs by their location on this diagram. We also plot the line fluxes determined from spectra averaged in five mass bins. The blue and red error bars are the formal and bootstrapped errors, respectively. The gray contours are the distribution of ~93,000 local galaxies in the SDSS. The red curve is the empirical separation between purely star-forming galaxies, and composites and AGNs in the local universe (Kewley et al. 2006). The blue curve is the separation at $z \sim 1.6$ (Kewley et al. 2013b).

(A color version of this figure is available in the online journal.)

AGNs. For our sample, we find that $8\% \pm 3\%$ are AGNs. This value is consistent with the estimates of Stott et al. (2013) for galaxies at $z \sim 1.5$.

We are not able to assess AGN contamination for the full sample since we have *J*-band observations and significant detection of [O III]λ6584 for only a fraction of our sample (72 out of 162). In order to assess the potential impact of AGN contamination on our measurement of the MZ relation, we determine the MZ relation for the 87 galaxies for which we have *J*- and *H*-band observations and compare it to the same sample with the six galaxies identified as AGNs removed. Figure 5 shows the MZ relation determined for the sample with (red points and curve) and without (black points and curves) the six galaxies identified as AGNs removed. In this *J*-band-observed subsample, AGN contamination leads to a slight overestimate of the metallicity for the least massive galaxies. However, the two relations are consistent within the observational errors and we conclude that AGN contamination is not significant in our sample. Throughout the rest of the paper, we remove the six galaxies identified as AGNs. The results presented in Section 5 are based on the analysis of 156 galaxies.

4.2. Metallicity Comparison

In Figure 6, we compare metallicities determined using the $N2$ and $O3N2$ diagnostics for the 81 galaxies for which we have both *J*-band and *H*-band spectroscopy. The data are sorted in the same manner as the previous section. The metallicities derived from the $O3N2$ diagnostic are systematically lower than those determined using the $N2$ diagnostic. This result is consistent
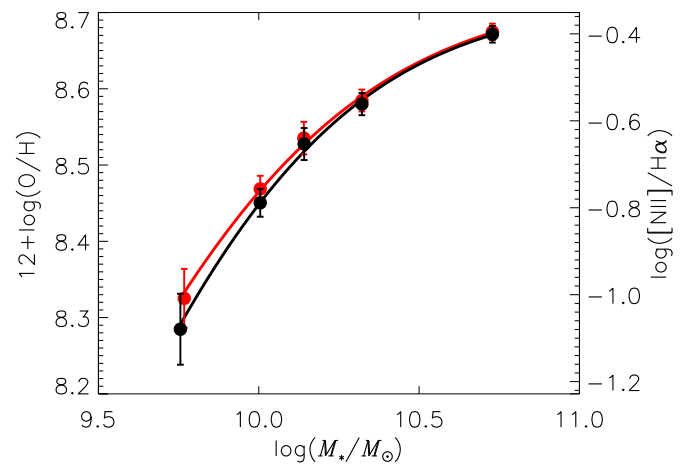

Figure 5. Comparison of the MZ relation for our sample of 87 galaxies with *J*- and *H*-band observations. The red curve is determined from the full sample and the black curve is determined from a subsample of 81 galaxies where the six galaxies identified as AGNs in Figure 4 are removed. The impact of AGN contamination appears to be negligible.

(A color version of this figure is available in the online journal.)

with Erb et al. (2006) and Yabe et al. (2012) who also find that the $O3N2$ diagnostic gives systematically lower metallicities than the $N2$ diagnostic in high-redshift galaxies.

The $O3N2$ and the $N2$ diagnostic of Pettini & Pagel (2004) are calibrated to the same data and in the local universe these two calibrations provide consistent results (e.g., Kewley & Ellison 2008). However, Figure 6 demonstrates that at higher
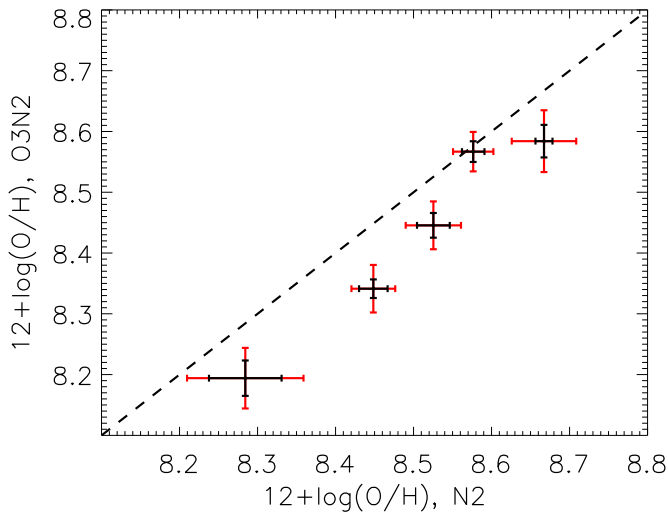
Figure 6. Comparison of the metallicity determined from the $N2$ and $O3N2$ calibration of PP04 for the subsample of our galaxies with both J- and H-band observations. The metallicities are determined from spectra averaged in five mass bins. The black and red error bars are the formal and bootstrapped errors, respectively. The dashed line is the one-to-one agreement.

(A color version of this figure is available in the online journal.)

Figure 7. Metallicity measured in individual galaxies as a function of stellar mass. The black data points are galaxies with [N II]$\lambda6584$ measured with S/N > 3. The red points are galaxies for which we have adopted 3σ upper limits for the [N II]$\lambda6584$ flux.

(A color version of this figure is available in the online journal.)

redshifts, the two diagnostics are not consistent. The offset is even larger when using the more recent calibration of the $O3N2$ and $N2$ diagnostic provided by Marino et al. (2013). The systematic offset in metallicity between the two diagnostics is attributed to changing physical conditions of the ISM in high-redshift galaxies (Erb et al. 2006; Kewley et al. 2013b; Cullen et al. 2014). In particular, a harder ionizing radiation field in high-redshift galaxies is consistent with the $O3N2$ systematically offsetting to lower metallicities when compared with $N2$ (L. Kewley et al., in preparation). In higher-redshift galaxies, the high sensitivity of the $O3N2$ diagnostic to the ionization parameter makes it a poor indicator of metallicity (L. Kewley et al., in preparation). The $N2$ diagnostic provides a more robust estimate and is the one adopted in this study. From our analysis, we conclude that the $O3N2$ diagnostic should not be used to determine metallicities for galaxies outside the local universe.

5. RESULTS

5.1. The Mass–Metallicity Relation

In Figure 7, we plot the metallicity as a function of stellar mass for individual galaxies in the sample. The metallicities are determined from the fitted $N2$ ratio using the PP04 calibration. The black points are the galaxies where [N II]$\lambda6584$ is measured with S/N > 3. The error bars only reflect the observational uncertainties and do not account for the 0.18 dex intrinsic dispersion of the metallicity calibration. The red points are galaxies for which we have adopted an 3σ upper limit for the [N II]$\lambda6584$ line flux. As Figure 7 demonstrates, we are more likely to not detect [N II]$\lambda6584$ in less massive galaxies. In Paper I, we show that the less massive galaxies in our sample have lower SFRs. The greater number of non-detections in less massive galaxies is likely due to their lower SFRs. Strong sky lines contaminate ~10% of the spectra and the small number of non-detections at higher stellar masses are likely due to strong sky line contamination.

Figure 7 shows that some less massive galaxies in our sample are metal-rich. The observed scatter in Figure 7 is the lower limit
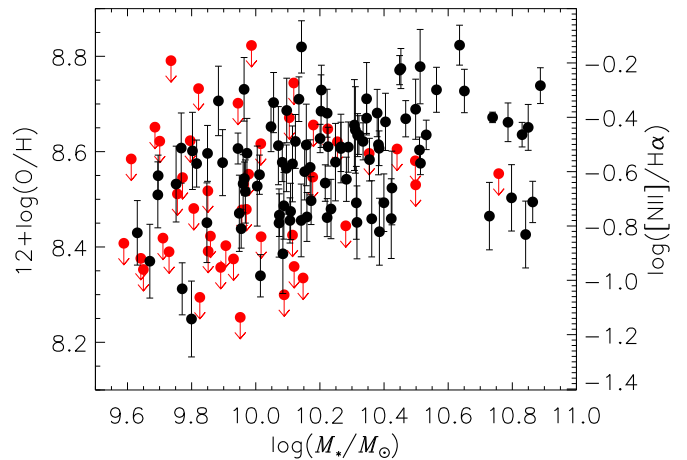
to the true scatter. Metal-rich galaxies are found across the whole stellar mass range probed in this study. This is consistent with the distribution of metal-rich galaxies observed in the local universe (Zahid et al. 2012a). It is important to note that we have adopted a 3σ upper limit for [N II]$\lambda6584$ in galaxies. The number of galaxies with upper limits on metallicity is substantially larger at the lower mass end of the distribution. This suggests that the scatter likely increases as a function of stellar mass (see also Zahid et al. 2012a). Here, we have used the $N2$ diagnostic for determining metallicity and it is important to bear in mind that saturation of the diagnostic likely contributes in part to the nearly constant upper metallicity envelope of the distribution in Figure 7.

Figure 7 demonstrates that our observations do not have sufficient sensitivity to provide an unbiased probe of metallicities in galaxies at stellar masses $M_* \lesssim 10^{10.3}\,M_\odot$. The S/N of [N II]$\lambda6584$ is a function of both SFR and metallicity. Since these physical properties are both strongly correlated with stellar mass, this leads to bias in the MZ relation determined from individual galaxies in our sample. We therefore rely on averaging spectra in order to increase the S/N of our measurement and determine a less biased MZ relation.

Our analysis is based on averaging spectra sorted into ten bins of stellar mass. There are 15 or 16 spectra in each of the mass bins. The stellar mass adopted is the median stellar mass in each bin. The metallicity is determined from the $N2$ line ratio determined from the averaged spectra shown in Figure 2. The Hα line is detected and SFRs are measured in individual objects without the necessity to stack (Paper I). The SFR adopted is the median SFR in each bin. The data are summarized in Table 1.

Figure 8 shows the MZ relation at $z \sim 1.6$ (black curve). The black points are the metallicities determined from the average spectra. The black error bars are the formal observational uncertainties determined by propagating the observational uncertainty in each pixel of the individual spectra. At a fixed stellar mass, there is intrinsic scatter in the metallicity distribution of galaxies (Tremonti et al. 2004; Zahid et al. 2012a). The red error bars are the standard deviation of the bootstrapped metallicity distribution in each bin of stellar mass and provide an estimate of the intrinsic scatter. Figure 8 shows that in each of the stellar mass bins the observational uncertainties are always smaller than the intrinsic scatter.
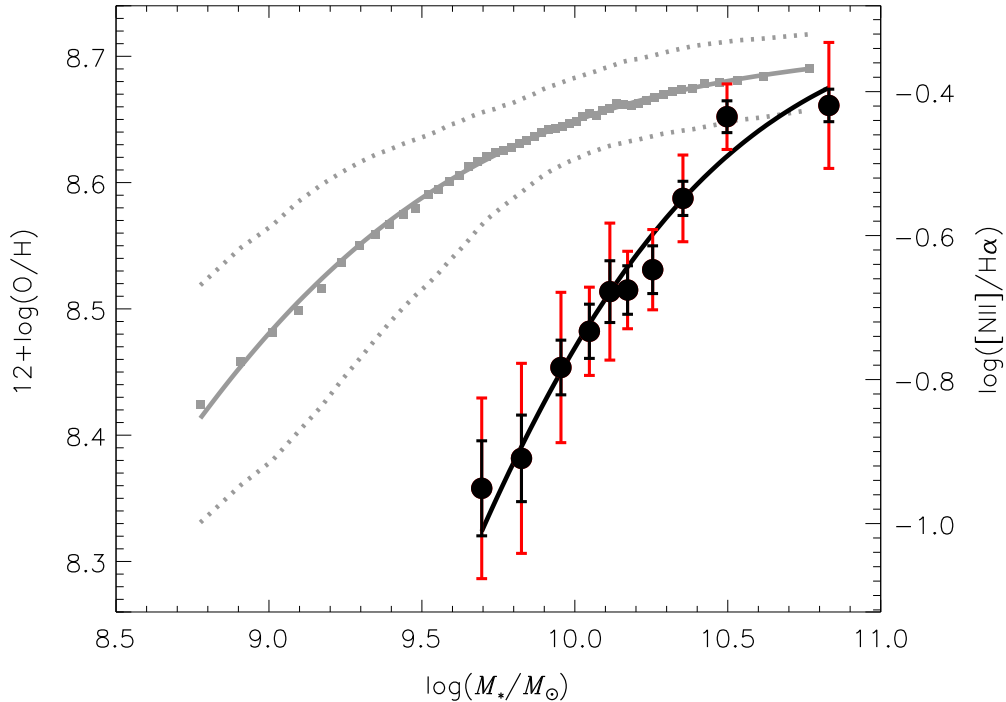
Figure 8. MZ relation determined from our sample of galaxies at $z \sim 1.6$. The black points are metallicities determined from spectra averaged in ten mass bins. The black and red error bars are the formal and bootstrapped errors, respectively. The black curve is a fit to the $z \sim 1.6$ MZ relation as described by Equation (6). The gray data points are the median metallicities in 50 bins of stellar mass for galaxies in our local fiducial sample from SDSS. The solid gray curve is a fit to the local relation and the dotted lines denote the interval containing the central 68% of the galaxies.

(A color version of this figure is available in the online journal.)

Table 2
MZ Relation Fit

Sample	Redshift	Z_o	$\log(M_o/M_\odot)$	γ
SDSS	0.08	8.710 ± 0.001	8.76 ± 0.01	0.66 ± 0.01
COSMOS	1.55	8.740 ± 0.042	9.93 ± 0.09	0.88 ± 0.18

Note. Fits shown in Figure 8 and parameterized by Equation (6).

We fit the MZ relation using the logarithmic form suggested by Moustakas et al. (2011). The MZ relation is parameterized as

$$12 + \log(\mathrm{O/H}) = Z_o - \log\left[1 + \left(\frac{M_*}{M_o}\right)^{-\gamma}\right]. \quad (6)$$

This function is preferred to a polynomial fit since it encapsulates much of our intuition regarding chemical evolution (see Moustakas et al. 2011; Zahid et al. 2013a). In this parameterization, Z_o is the asymptotic metallicity where the MZ relation flattens, M_o is the characteristic stellar mass where the relation begins to flatten, and γ is the power-law slope of the MZ relation for stellar masses $\ll M_o$. The parameters are determined using a χ^2 minimization as implemented in the *MPFIT* package in IDL (Markwardt 2009). The MZ relation at $z \sim 1.6$ is shown by the black curve. We derive the local MZ relation by sorting the data into 50 bins of stellar mass and taking the median metallicity in each bin. The error bars are smaller than the data points. The dotted curves contain the central 68% of the galaxy distribution. We determine the MZ relation for the local sample using the same diagnostic (i.e., $N2$ calibrated by PP04) as applied to the $z \sim 1.6$ data. The observational uncertainties are propagated through and the fit parameters and errors are given in Table 2.

In Section 4.1 and Figure 5, we examine the MZ relation for our subsample for which we have *J*-band observations and are able to assess AGN contamination. The black curve in Figure 5 is the MZ relation with six galaxies identified as AGNs removed from the sample. The fit to the MZ relation in Figure 5 is consistent with the relation we derive in Figure 8.

5.2. The Stellar Mass, Metallicity, and SFR Relation

The metallicities of galaxies are governed by gas flows and star formation. Recent work shows that in local galaxies there appears to be an *anti*-correlation between the SFR and metallicity at a fixed stellar mass (Ellison et al. 2008; Mannucci et al. 2010; Andrews & Martini 2013); at least at lower stellar masses (see Yates et al. 2012). One possible explanation for this trend is that while inflows of gas dilute the gas-phase abundance and lower metallicities, they also fuel star formation and lead to elevated SFRs. Motivated by this physical picture, Mannucci et al. (2010) propose that the parameterization of the relation between stellar mass, metallicity, and SFR that minimizes the scatter in local galaxies is independent of redshift. They refer to this as the "fundamental metallicity relation" (FMR). In their analysis, the lower metallicities of intermediate and high-redshift galaxies are compensated by their higher SFRs such that galaxies out to $z \sim 2.5$ are consistent with local FMR. However, it is clear that the FMR is highly dependent on methodology (Yates et al. 2012; Andrews & Martini 2013). Therefore, applying a consistent methodology is important. We determine stellar masses, metallicities, and SFRs for local galaxies and our sample at $z \sim 1.6$ by applying as consistent a methodology as is currently possible in order to test the validity of the FMR.

The scatter in the local MZ relation is correlated with the SFR (Ellison et al. 2008; Mannucci et al. 2010; Yates et al. 2012;
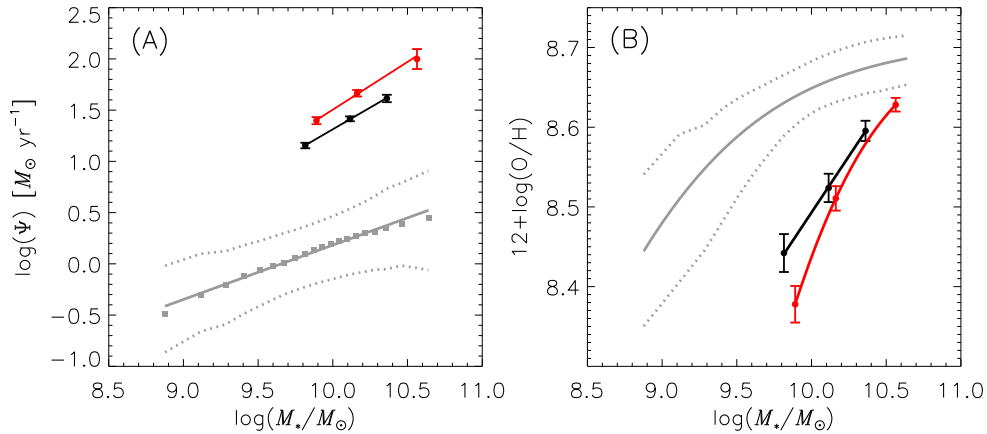
Figure 9. (A) Relation between stellar mass and SFR. The black and red points are the median SFRs for galaxies that are first sorted into three mass bins and then two SFR bins. The solid black and red lines are linear fits to the relation between stellar mass and SFR for the high and low SFR bins, respectively. The gray points are the median SFRs sorted into 50 bins of stellar mass for star-forming galaxies in our local fiducial sample. The solid line is a fit to the relation between stellar mass and SFR, and the dotted line denotes the interval containing the central 68% of galaxies. (B) The MZ relation for the sample divided into bins of stellar mass and SFR for the same data shown in (A). The black and red points are the metallicities in bins of stellar mass and SFR. The black and red curves are fits to the high and low SFR data, respectively. The gray curve is the fit to the local MZ relation and the dotted line denotes the interval containing the central 68% of galaxies.

(A color version of this figure is available in the online journal.)

Table 3
FMOS-COSMOS Stellar Mass, Metallicity, and SFR Relation

Stellar Mass $\log(M_*/M_\odot)$	N2 $\log([\text{N\,II}]/\text{H}\alpha)$	12+log(O/H) PP04	$\log(\Psi)$ $(M_\odot\ \text{yr}^{-1})$	N
		Low-SFR		
9.82	-0.803 ± 0.042	8.442 ± 0.024	1.155 ± 0.027	26
10.11	-0.660 ± 0.031	8.524 ± 0.018	1.415 ± 0.023	26
10.36	-0.534 ± 0.022	8.595 ± 0.013	1.614 ± 0.034	26
		High-SFR		
9.89	-0.916 ± 0.040	8.378 ± 0.023	1.397 ± 0.033	26
10.16	-0.683 ± 0.027	8.511 ± 0.015	1.665 ± 0.031	26
10.56	-0.477 ± 0.015	8.628 ± 0.009	1.999 ± 0.090	26

Note. The same as Table 1 but split into two bins of SFR as described in the text.

Andrews & Martini 2013). We can examine the relation between stellar mass, metallicity, and SFR for our sample at $z \sim 1.6$ because we have SFRs determined from the Hα luminosity in individual galaxies. We average the spectra by first sorting the data into three bins of stellar mass and then dividing the data in each bin of stellar mass into two bins of SFR. The metallicity and SFR in each bin of stellar mass and SFR is determined from 26 galaxies.

In Figure 9 we examine the relation between stellar mass, metallicity, and SFR. The data shown in Figure 9 are given in Table 3. In Figure 9(A), we plot the median SFR in each bin. The error bars are the bootstrapped errors on the median and are analogous to the standard error on the mean. The red and black curves in Figure 9 are linear fits with a slope of 0.93 ± 0.13 and 0.85 ± 0.08, respectively. The local stellar mass–SFR relation is shown in gray. The local relation is determined by taking the median SFR in 50 bins of stellar mass. The solid gray line is a fit to the local relation. The dotted gray curves indicate the limits containing the central 68% of the galaxy distribution. The slope of the local relation is 0.68 ± 0.01 and does not differ significantly (2σ) from the slope of the $z \sim 1.6$ relation. However, the slope of the relation is dependent on sample selection (cf. Peng et al. 2010).

In Figure 9(B), we show the MZ relation for the data sorted into bins of SFR. The MZ relation shown by the red

and black curves corresponds to the high and low SFR bins, respectively, shown in Figure 9(A). The gray curve is the local MZ relation. The metallicities of high SFR galaxies (red curve) are systematically lower than the metallicities of low SFR galaxies (black curve). At a fixed stellar mass, the metallicity is *anti*-correlated to the SFR. This is similar to trends seen in local galaxies at lower stellar masses (e.g., Mannucci et al. 2010). It is important to note that while the slope of the stellar mass–SFR relation is similar for local and $z \sim 1.6$ galaxies, the MZ relation for the same galaxies is significantly steeper. This has important implications for the FMR proposed by Mannucci et al. (2010). We examine this issue in detail in Section 7.3.

5.3. The Stellar Mass, Metallicity, and $E(B-V)$ Relation

A strong correlation is observed between metallicity and dust in the local universe (Heckman et al. 1998; Boissier et al. 2004; Asari et al. 2007; Garn & Best 2010; Xiao et al. 2012; Zahid et al. 2012b, 2013c). Reddy et al. (2010) indirectly examine the relation between dust obscuration and metallicity at $z \sim 2$. They find that the $L_{\text{IR}}/L_{\text{UV}}$ ratio, which is taken as a proxy for dust, scales with stellar mass. They combine the relation between the stellar mass and $L_{\text{IR}}/L_{\text{UV}}$ ratio with the relation between stellar mass and metallicity from Erb et al. (2006) to derive a relation between the metallicity and $L_{\text{IR}}/L_{\text{UV}}$ ratio, i.e., dust extinction.

In Figure 10, we examine the relation between stellar mass, metallicity, and $E(B-V)$. The data shown in Figure 10 are given in Table 4. We average the spectra by first sorting the data into three bins of stellar mass and then divide the data in each bin of stellar mass into two bins of $E(B-V)$. The metallicity and $E(B-V)$ in each bin is determined from 26 galaxies. In Figure 10(A), the $E(B-V)$ value is the median of the 26 galaxies in each bin and the errors are bootstrapped. The red and black points correspond to the high and low $E(B-V)$ bins, respectively. The gray squares are the median $E(B-V)$ values in 50 bins of stellar mass for the local sample of galaxies. The dotted lines denote the interval containing 68% of the galaxy distribution.

In Figure 10(B), we plot the metallicity determined in bins of stellar mass and $E(B-V)$. The red and black points and curves correspond to the high and low $E(B-V)$ sample, respectively. Figure 10(B) shows that galaxies with higher $E(B-V)$ (red
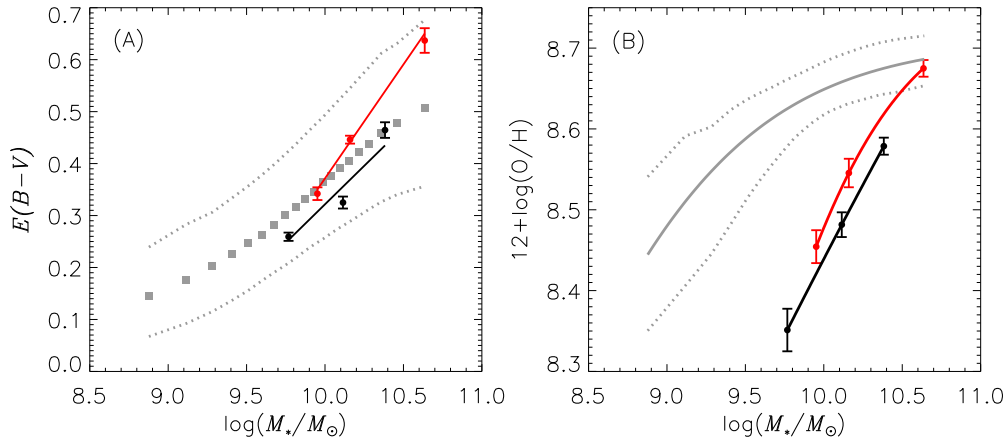
Figure 10. (A) Relation between stellar mass and $E(B-V)$. The black and red points are the median nebular $E(B-V)$ for galaxies that are first sorted into three mass bins and then two $E(B-V)$ bins. The solid black and red lines are linear fits to the relation between stellar mass and $E(B-V)$ for the high and low $E(B-V)$ bins, respectively. The gray points are the median $E(B-V)$ sorted into 50 bins of stellar mass for star-forming galaxies in our local fiducial sample. The solid line is a fit to the relation between stellar mass and SFR, and the dotted lines denote the interval containing the central 68% of the galaxies. (B) The MZ relation for the sample divided into bins of stellar mass and $E(B-V)$ for the same data shown in (A). The black and red points are the metallicities in bins of stellar mass and $E(B-V)$. The black and red curves are fits to the high and low SFR data, respectively. The gray curve is the fit to the local MZ relation and the dotted line denotes the interval containing the central 68% of the galaxies.

(A color version of this figure is available in the online journal.)

Table 4
FMOS-COSMOS Stellar Mass, Metallicity, and $E(B-V)$ Relation

Stellar Mass $\log(M_*/M_\odot)$	N2 $\log([\text{N\,II}]/H\alpha)$	12+log(O/H) PP04	$E(B-V)$ Nebular	N
		Low-$E(B-V)$		
9.77	-0.963 ± 0.046	8.351 ± 0.026	0.259 ± 0.008	26
10.11	-0.734 ± 0.027	8.482 ± 0.015	0.325 ± 0.012	26
10.38	-0.564 ± 0.019	8.579 ± 0.011	0.464 ± 0.015	26
		High-$E(B-V)$		
9.95	-0.782 ± 0.036	8.454 ± 0.020	0.342 ± 0.012	26
10.16	-0.622 ± 0.031	8.545 ± 0.018	0.446 ± 0.008	26
10.64	-0.395 ± 0.018	8.675 ± 0.010	0.637 ± 0.024	26

Note. Same as Table 1, but split into two bins of $E(B-V)$ as described in the text.

points) also have higher metallicity. At a fixed stellar mass, the metallicity is correlated with dust extinction. Similar trends are observed in the local sample (e.g., Zahid et al. 2012b, 2013c). This correlation is perhaps not that surprising since dust is composed of metals.

6. SYSTEMATIC ISSUES IN THE MEASUREMENTS

Before turning to a discussion of our results, we highlight some of the systematic issues in our measurements. Current and future spectroscopic surveys should be able to address many of these issues.

The fit to the MZ relation presented in Section 5.1 is strongly constrained by the two highest stellar mass bins. In Figure 8, the bin at $M_* \sim 10^{10.5} M_\odot$ is above the relation. Figure 7 shows that there is a lack of intermediate and low metallicity objects for galaxies in this mass range. If we exclude the bin at $M_* \sim 10^{10.5} M_\odot$, the fitted Z_o and $\log(M_o/M_\odot)$ are 8.75 ± 0.06 and 9.94 ± 0.15, respectively. These values are consistent with values given in Table 2. Excluding the second to highest stellar mass bin in our fit does not change any of the conclusions of this paper. However, if we exclude the highest stellar mass bin, the two fits are not consistent. The saturation metallicity, Z_o, and

turnover mass, M_o, are both strongly dependent on the highest mass bin.

Our analysis of AGN contamination presented in Figure 4 suggests that AGN contamination does not significantly affect our measurement of the MZ relation. Similarly, Wuyts et al. (2014) find that the MZ relations they measure at $z \sim 1$ and $z \sim 2$ are insensitive to AGN contamination. This might be due to evolving ISM conditions, which may result in a BPT diagram where the [N\,II]/Hα line ratios of AGN overlap with star-forming galaxies (e.g., Kewley et al. 2013a, 2013b). Whatever the case, Figure 4 and results from Wuyts et al. (2014) suggest that AGN contamination is not a significant source of bias.

Our sample presented here is selected primarily using the sBzK selection in order to maximize detections. In Paper III, we show that the sBzK sample spans the same color space as a sample selected on the basis of full spectral energy distributions. There does not seem to be a serious bias with the sBzK sample that would affect the metallicity. In Paper III, we show that the sBzK selection produces a narrower main sequence. This may decrease some of the dispersion in the intrinsic properties of the sample, but should not cause any systematic offset that could change the slope of the MZ relation.

While the sBzK selection is not significantly biased against dusty galaxies because the reddening vector moves objects parallel to the selection cut (Daddi et al. 2004), our effective sensitivity of 4×10^{-17} erg s^{-1} cm^{-2} may not reach deep enough to observe Hα in objects that are heavily obscured by dust. To increase the likelihood of detection, for the majority of the sample, we imposed a second selection criteria that required obscured SFRs of $\sim 5 M_\odot$ yr^{-1} based on UV luminosities. This introduces bias against heavily obscured objects. In Figure 10, we show that the metallicity is correlated with dust extinction. Thus, if our sample is biased against heavily obscured objects, we may be missing many metal-rich galaxies in our sample $z \sim 1.6$. This bias is likely to be mass-dependent and effect our measurement of the MZ relation at high stellar masses. A correction for this bias would not lower the slope of the MZ relation. However, galaxies with heavy dust obscuration also tend to have higher SFRs. The relation between SFR and

metallicity is opposite to the relation between dust extinction and metallicity and therefore these two effects may offset each other. The relation between stellar mass, metallicity, dust extinction, and SFR is complicated and larger spectroscopic samples are required in order to assess any bias that may be present in our measurements.

The observed anti-correlation between metallicity and SFR (e.g., Mannucci et al. 2010) may lead to an overestimate of the MZ relation at low stellar masses. This is because the galaxies with SFRs falling below our detection limit are preferentially found at lower stellar masses and, because of the anti-correlation between metallicity and SFR, these low SFR galaxies also tend to have high metallicities. This type of bias would effect the lowest stellar mass bins resulting in an artificial steepening of the MZ relation. However, the SFRs we measure show the same amount of scatter at low and high stellar masses (see Kashino et al. 2013) and our K-band selection limit is designed to select galaxies with stellar masses where the SFRs are detectable. While the distribution of SFRs we measure is slightly narrower than previous studies (see Kashino et al. 2013 for discussion), the survey is designed such that we are not missing a significant number of galaxies with low SFRs. Thus, this type of bias is unlikely to significantly change the slope we measure.

One of the primary challenges with spectroscopically accessing the redshift desert ($1 \lesssim z \lesssim 2$) is that optical emission lines are redshifted into the near-infrared. The near-infrared is significantly contaminated by strong atmospheric emission lines, making observations of faint emission lines extremely difficult. This is compounded by detector throughput and sensitivities that are significantly below optical detectors. Because of these difficulties, we are not able to observe faint emission lines such as [N II]$\lambda 6584$ in a significant number of individual galaxies. Instead, we must rely on averaging many spectra in order to achieve the S/N necessary to detect weak emission lines. This may be problematic since the properties of galaxies that we are measuring are not necessarily linear with line strength. For example, the [N II]$\lambda 6584$ line strength scales exponentially with metallicity and therefore simply averaging spectra may bias our measurement.

To address the issue of stacking, we have measured the relation using the median of the stacked spectra, rather than average to test for any systematic bias. The two methods yield consistent results. Additionally, we examine the bias in local star-forming galaxies by sorting galaxies into 50 bins of stellar mass and then averaging the line flux of [N II]$\lambda 6584$ and Hα *before* determining metallicity. Thus, we determine the MZ relation from the average [N II]$\lambda 6584$ and Hα flux. We find a very small offset (~ 0.01 dex) between the two methods. In Geller et al. (2014), we measure the MZ relation determined from stacked spectra using the R23 diagnostic, and compare it to the MZ relation we derive in Zahid et al. (2013a) from individual galaxies (see Figure 16 of Geller et al.). The stacked data give results consistent with measurements of the MZ relation derived from individual galaxies. We conclude that the MZ relation derived from stacked data is consistent with the MZ relation derived from individual galaxies.

For many objects, the redshift is determined from a single emission line. In Paper III, we compare our redshifts with the zCOSMOS spectroscopic redshift survey (Lilly et al. 2007). There are 37 objects in both catalogs, which allow us to assess the accuracy of our redshift determination. We find that 33/37 objects (89%) yield consistent redshifts. Some fraction of the inconsistent redshifts are due to errors in the zCOSMOS

assignment. We conclude that misidentification affects $\lesssim 10\%$ of the sample. Misidentification of an emission line results in an underestimate of the [N II]$\lambda 6584$ flux relative to Hα since there is no corresponding [N II]$\lambda 6584$ emission. Assuming that [N II]$\lambda 6584$ fluxes are distributed about the mean, we estimate that the misidentification fraction translates directly into the fractional underestimate of the average flux measured in our stacked data. A $\lesssim 10\%$ error in [N II]$\lambda 6584$ flux translates to a $\lesssim 0.03$ dex underestimate of the uncertainty. This level of contamination does not change any of the major conclusions of this work.

We have used the local calibrations for metallicity and applied them to high-redshift data. Several authors have shown that evolving ISM conditions may lead to evolution in key emission line diagnostics (Erb et al. 2006; Hainline et al. 2009; Rigby et al. 2011; Yabe et al. 2012; Kewley et al. 2013a). Typically, these studies have argued for evolving ISM conditions on the basis of the [O III]/Hβ versus [N II]/Hα diagram. However, the metallicities of galaxies are also dependent on conditions of the ISM (e.g., Kewley & Dopita 2002). In this study, we have shown that the metallicities determined using the $N2$ and $O3N2$ line ratios are inconsistent despite being calibrated to the same data in the local universe (PP04). In order to assess the impact of these variations on metallicity, deep observations of full optical spectra in a large sample of galaxies are necessary.

In Zahid et al. (2013a), we attribute the flattening of the MZ relation for massive galaxies to the physical effect of metallicity saturation. In that study, we determine metallicities using the $R23$ diagnostic. Photoionization modeling suggests that this metallicity diagnostic saturates at metallicities significantly higher than the maximum metallicity observed in star-forming galaxies (Kewley & Dopita 2002). However, the $N2$ diagnostic is prone to saturation at significantly lower metallicities (Kewley & Dopita 2002). The saturation of $N2$ suggests that metallicities may be higher than those that we have measured here. However, we emphasize that the flattening observed in the local MZ relation is present using several different diagnostics (see Kewley & Ellison 2008). Moreover, the high $N2$ ratios are only observed in the most massive galaxies and therefore saturation may only effect a small fraction of the most massive galaxies. Since we have applied the same diagnostic to both our local and $z \sim 1.6$ samples, we have mitigated uncertainties in the relative metallicities.

In Figure 9, we examine the relation between stellar mass, metallicity, and SFR. Similar to the local universe, there appears to be an anti-correlation between metallicity and SFR at a fixed stellar mass. We measure SFR from the Hα line flux and metallicity is determined from the $N2$ ratio. While SFR is directly dependent on the Hα line flux, the metallicity is inversely dependent on the Hα line flux. The errors are correlated in the same way as the observed trends. This could potentially produce an artificial trend in our measurement of the stellar mass, metallicity, and SFR relation for galaxies at $z \sim 1.6$. However, we note that for local galaxies, such trends persist even when completely independent line diagnostics are used. For example, similar trends are observed when SFRs are determined from Balmer lines and metallicities are determined from the [N II]$\lambda 6584$/[O II]$\lambda 3727$ ratio (Andrews & Martini 2013). In this case, the two measurements are independent and the effect in local galaxies cannot be attributed to correlated errors. It remains to be seen whether trends persist when using independent diagnostics for higher redshift samples.
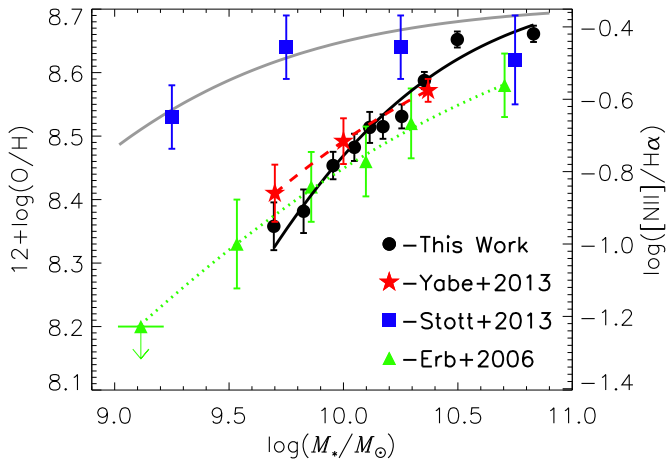
Figure 11. Comparison of the MZ relation that we measure at $z \sim 1.6$ with the measurement at $z \sim 1.4$ from Yabe et al. (2012). The black filled circles and curve are our measurements, and the red stars are measurements from Yabe et al. (2012).

(A color version of this figure is available in the online journal.)

In Figure 10, we examine the relation between stellar mass, dust extinction, and metallicity. The trends observed in the relation at $z \sim 1.6$ are similar to those observed in local galaxies. Namely, at a fixed stellar mass, dust extinction is correlated to metallicity. However, we are currently not able to apply a consistent methodology when examining these two samples because Hβ is detected in only a small fraction of our sample. We instead rely on dust extinction determined from the continuum extinction measured from the $B-z$ color. We convert this to nebular extinction using the factor we derive in Paper I. While this may apply to population on average, this may not be applicable to individual galaxies. Future surveys with higher sensitivity and broader wavelength coverage should be able to establish the validity of this approach and robustly establish the relation between stellar mass, dust extinction, and metallicity.

7. DISCUSSION

7.1. Comparison of the MZ Relation with Previous High-z Studies

Yabe et al. (2012) report on the MZ relation at $z \sim 1.4$ based on FMOS observations conducted in low-resolution mode. The initial sample is K-band selected with a secondary selection for galaxies expected to have Hα flux $> 10^{-16}$ erg s^{-1} cm^{-2} based on rest-frame UV emission. They derive an MZ relation by stacking the spectra of 71 galaxies that have significant Hα detections in three mass bins. In order to make a robust comparison, both the stellar masses and metallicities must be determined in a consistent manner. Yabe et al. (2012) derive metallicities from the $N2$ using the PP04 calibration. However, we find that the stellar mass estimates are systematically offset mostly (but not completely) due to the different IMFs adopted. We recalculate the stellar masses applying our methodology using photometry provided by K. Yabe. We compare our derived stellar masses with those calculated by Yabe et al. (2012). Our mass estimates are systematically lower by 0.28 dex. For consistency, we subtract 0.28 dex from the stellar masses derived by Yabe et al. (2012) when plotting the MZ relation.

Figure 11 shows a direct comparison between the MZ relation derived by Yabe et al. (2012, red stars) and the MZ relation

that we measure (black solid curve and filled circles). Our data extend ~ 0.5 dex higher in stellar mass. The MZ relation we derive is systematically steeper, though over the stellar mass range probed by Yabe et al. (2012) the metallicities in the individual bins are consistent within the errors. As we noted in Section 6, some small fraction of the galaxies have misidentified Hα. Including these galaxies in the average leads to an underestimate of the metallicity. The misidentification of Hα largely effects the least massive galaxies in the sample. This may explain the lower metallicities that we measure in the lowest mass bin. Given the differences in sample size (156 compared to 71 galaxies) and observational modes (high resolution compared to low resolution) we consider the good agreement in the two measurements to be reassuring.

In Figure 11, we also plot the MZ relation from Erb et al. (2006, green triangles). Erb et al. (2006) average the spectra of 87 star-forming galaxies at $z \sim 2.3$ in five bins of stellar mass. We have recalculated their stellar masses using the same methodology applied to our $z \sim 1.6$ sample in order to ensure a consistent comparison (see Zahid et al. 2012b). The Erb et al. (2006) sample is flatter than the relation we derive for our sample at $z \sim 1.6$. At the low mass end, our metallicities may be underestimated. This may explain part of the discrepancy (see Section 6). At the high mass end, it is possible that metallicities determined by Erb et al. (2006) may be underestimated. The sample of Erb et al. (2006) is UV selected Lyman break galaxies and therefore biased against dusty objects. In Figure 10, we show that dust extinction and metallicity are correlated. The UV selected samples are likely to be missing the dustier, metal-rich massive galaxies and therefore the average metallicity derived by Erb et al. (2006) may be underestimated in the highest mass bins.

Henry et al. (2013) have examined the MZ relation for low mass galaxies at $z \sim 1.8$. The data demonstrate a clear decline in metallicity at lower stellar masses (down to $\sim 10^8 M_\odot$). The relation they derive is consistent with our measurements. However, we note that due the faintness of low mass galaxies, the observational uncertainties are large and therefore do not provide a strong validation of the MZ relation we derive.

Recently, Stott et al. (2013) report an MZ relation for a combined sample of galaxies at $z = 0.84$ and $z = 1.47$. They determine the metallicity from stacking spectra 103 galaxies into four bins of stellar mass. The blue squares in Figure 11 are their measurements of the MZ relation. The primary conclusion of Stott et al. (2013) is that the MZ relation does not evolve with redshift (compare their data with the local relation shown by the gray curve in Figure 11). They argue that the more than dozen previous studies reporting an evolution in the MZ relation are biased. They cite the higher SFRs probed in previous studies and selection bias in UV-selected samples as the origin of the reported evolution.

Figure 11 clearly demonstrates that the lack of evolution in the MZ relation reported by Stott et al. (2013) is not supported by our data. The potential sources of bias provided by Stott et al. (2013) do not strictly apply to our data. Our sample is based on the sBzK selection, which is significantly less biased against dusty objects as compared to UV selections. This is because in color–color space, the effect of dust is to move objects parallel to the selection criteria (Daddi et al. 2004). Furthermore, this effect should be most pronounced for massive galaxies and low mass galaxies are unlikely to be severely dust obscured. A second source of bias suggested by Stott et al. (2013) is that previous studies probe significantly higher average SFRs. We note that

our observations are carried using FMOS on Subaru operated in high-resolution mode. This setup is identical to the observational setup used by Stott et al. (2013). However, our observations are significantly deeper because we observe a single pointing position per night, whereas Stott et al. (2013) observed six positions in a night. Our observations have a sensitivity limit that is nearly an order of magnitude deeper than the observations of Stott et al. (2013) and therefore we are able to observe galaxies with significantly lower SFRs. We conclude that our sample does not suffer significantly from the type of bias suggested by Stott et al. (2013). We consider the redshift evolution of the MZ relation to be real.

7.2. Evolution of the MZ relation

In Zahid et al. (2013a), we examine the evolution of the MZ relation. Our analysis is primarily based on three large samples at $z < 1$ for which we are able to measure metallicities in individual galaxies using the same metallicity calibration (i.e., Kobulnicky & Kewley 2004). In Zahid et al. (2013a), we fit the MZ relation using the parameterization given in Equation (6) and conclude that the shape of the MZ relation evolves significantly with redshift such that it flattens at late times. In an "open-box" model of galaxy chemical evolution where star formation is primarily fueled by cosmological accretion and is capable of driving large scale galaxy winds that expel metals from the ISM, the gas-phase oxygen abundance may not exceed the effective yield.[26] We argue that the flattening of the MZ relation is primarily driven by massive galaxies enriching to the effective yield. We show that the upper metallicity limit, Z_o, does not evolve significantly out to *at least* $z \sim 0.8$ (Zahid et al. 2013a). Furthermore, we show that the flattening of the relation can be primarily understood as an evolution in M_o, the stellar mass at which the MZ relation begins to flatten. M_o is $\sim$0.7 dex lower in the local universe as compared to $z \sim 0.8$ (Zahid et al. 2013a).

The MZ relation that we derive at $z \sim 1.6$ is consistent with the evolution observed in the MZ relation at $z < 1$. Table 2 gives the fit parameters for the local and $z \sim 1.6$ relation.[27] Within the observational uncertainties, the saturation metallicity, Z_o, does not evolve since $z < 1.6$ and M_o is $\sim$1.2 dex larger at $z \sim 1.6$. The lack of evolution in the saturation metallicity places constraints on the metallicity of outflows and oxygen yields in star-forming galaxies. Detailed comparison of the evolution with analytical and numerical models is needed to rigorously establish this. The lack of evolution in Z_o and the evolution of M_o to larger masses means that only the most massive galaxies at $z \sim 1.6$ achieve the level of enrichment observed in the local universe. However, our interpretation remains tentative due to possible saturation of the $N2$ diagnostic (see Section 6).

The high gas-phase abundance of massive star-forming galaxies at $z \sim 1.6$ is consistent with observations, which indicates super-solar metallicities for the stellar populations of massive early-type galaxies (e.g., Gallazzi et al. 2005; Thomas et al. 2005; Panter et al. 2008; Conroy et al. 2014). Analysis of the

stellar population ages of these massive early-type galaxies indicates old stellar populations ($\gtrsim$10 Gyr). This implies that these galaxies formed stars in the distant past from gas-enriched to the level observed in massive star-forming galaxies in the local universe. More to the point, Panter et al. (2008) show that the most massive early-type galaxies exhibit super-solar stellar metallicities that do not evolve out to $z \gtrsim 2$. In contrast, less massive galaxies show significant evolution since $z \sim 2$ with the least massive galaxies showing the greatest evolution. The stellar metallicity evolution trends observed by Panter et al. (2008) are consistent with the evolution observed in the gas-phase oxygen abundance of the star-forming galaxy population since $z \sim 1.6$, i.e., a steepening of the MZ relation at higher redshift. The chemical evolution of star-forming galaxies may be characterized by an upper metallicity limit that does not evolve with redshift. This upper limit is achieved in progressively lower stellar mass galaxies as the universe evolves. This evolution is likely driven by the decreasing gas fraction of galaxies with time.

7.3. The Stellar Mass, Metallicity, and SFR Relation

Ellison et al. (2008) first showed the *anti*-correlation between specific SFR and metallicity at fixed stellar masses. Subsequently, this relation has been examined by several authors (e.g., Mannucci et al. 2010; Yates et al. 2012; Andrews & Martini 2013, and others). These studies show that, for SDSS galaxies, the scatter around the MZ relation is somehow correlated to the SFR. In particular, Mannucci et al. (2010) find that at a fixed stellar mass, the metallicity is *anti*-correlated to the SFR. They parameterize the metallicity as a function of stellar mass and SFR, i.e., $\mu_\alpha = \log(M_*/M_\odot) - \alpha\log(\Psi)$. They find that $\alpha = 0.32$ minimizes the scatter in the local MZ relation. They argue that the relation between metallicity and μ_α does not evolve for galaxies with $z < 3$ and refer to this relation as the FMR. For the FMR, the lower metallicities observed in high-redshift galaxies are compensated by their higher SFRs. However, the relation is dependent on methodology (Yates et al. 2012; Andrews & Martini 2013). There is no consensus regarding the evolution of the relation between stellar mass, metallicity, and SFR and therefore the validity of the FMR remains tentative (e.g., Niino 2012; Pérez-Montero et al. 2013; Sánchez et al. 2013; Cullen et al. 2014).

The analysis of the FMR we present differs from Mannucci et al. (2010) in one significant manner. Unlike Mannucci et al. (2010), who determine SFRs from dust-corrected Hα luminosity in the fiber, we instead adopt the aperture and dust-corrected SFRs provided by the MPA/JHU group in the SDSS DR7. This is very important as aperture corrections for SFRs are significant for local galaxies (see Zahid et al. 2013c). For the SDSS sample used in this study, the aperture-corrected SFRs are on average 0.5 dex larger than SFRs determined from Hα flux measured in the aperture. This is because the typical fiber covering fraction for galaxies in our local sample is $\sim$30%. For the Mannucci et al. (2010) sample, the average difference is 0.7 dex. The larger difference is because they do not apply a minimum covering fraction in selecting their sample. This difference is significant and substantially impacts the FMR. The FMR with aperture-corrected SFRs is offset by 0.22 dex from the FMR determined using SFRs calculated from the Hα flux in the fiber.

If we calculate metallicities for our sample using the Maiolino et al. (2008) $N2$ calibration, which is the one used in Mannucci et al. (2010), and apply the exact same selection and methodology in analyzing the local SDSS sample as Mannucci et al.

---

[26] The nucleosynthetic yield is the mass of oxygen formed per unit SFR. In the presence of outflows, some metals may be lost and the effective yield is the mass of oxygen produced minus the mass of oxygen lost in the wind per unit SFR.

[27] The fit parameters given in Table 2 cannot be directly compared to those provided in Zahid et al. (2013a). Because of the different spectral ranges covered by the data, we are required to apply different metallicity calibrations in determining metallicities. Systematic differences between various metallicity calibrations are well-documented, though relative metallicities are found to be robust (e.g., Kewley & Ellison 2008).
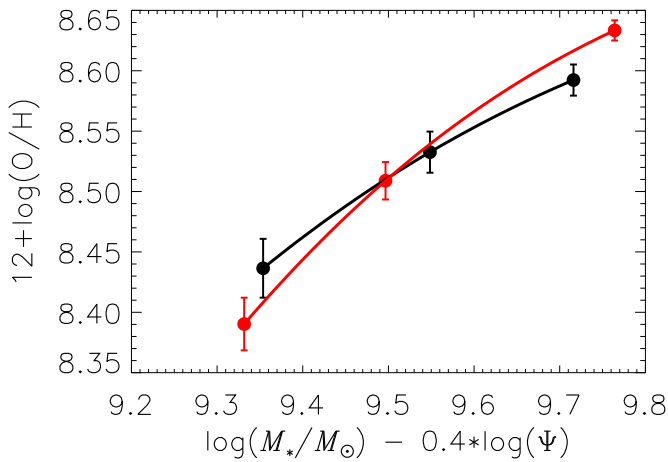
Figure 12. Following the approach of Mannucci et al. (2010), we plot metallicity against the combination of stellar mass and SFR that minimizes the scatter for our sample at $z \sim 1.6$. The data are the same as in Figure 9.

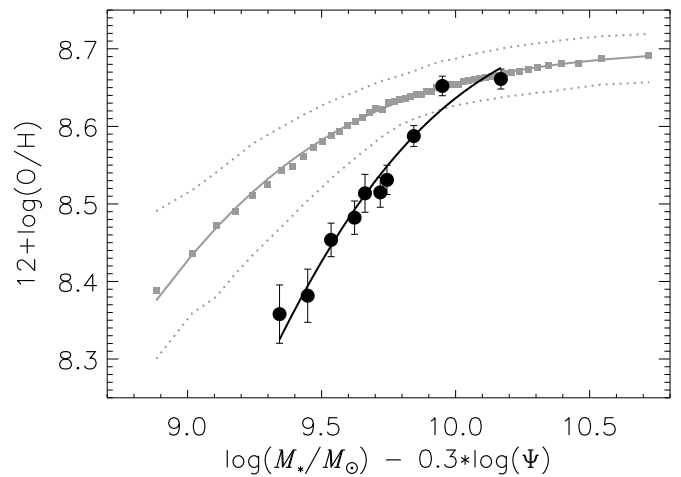(A color version of this figure is available in the online journal.)

Figure 13. FMR for our local fiducial sample (gray curve and squares) and our $z \sim 1.6$ sample (black curve and circles). The gray dotted lines denote the interval containing the central 68% of local galaxy distribution.

(2010), we find significantly better agreement between galaxies in the local universe and at $z \sim 1.6$. However, we still find that the sample at $z \sim 1.6$ is a steeper relation that is not fully consistent with the local FMR within the errors. The standard interpretation of the FMR is that it reflects short timescale responses to gas flows (Mannucci et al. 2010). Inflows of pristine gas decrease the gas-phase oxygen abundance, but also lead to an increase in SFR. In this sense, it is a relation between global, integrated properties of galaxies. However, the SDSS SFRs measured without aperture corrections are not reflective of the global SFR in SDSS galaxies and therefore not the appropriate measurement for deriving relations based on global properties. It is beyond the scope of this paper to examine the FMR in detail. We simply note that if we use SDSS SFRs without aperture corrections, we find better agreement between the local FMR and the relation at $z \sim 1.6$. This agreement is likely to be misleading. For the following analysis, however, we use the aperture-corrected SDSS SFRs.

In Figure 9, we examine the relation between stellar mass, metallicity, and SFR. Similar to trends reported by Mannucci et al. (2010 and others) for local SDSS galaxies, we find that, at a fixed stellar mass, metallicity is *anti*-correlated to the SFR. Following the approach of Mannucci et al. (2010), we determine the value, α, that minimizes the scatter in metallicity for our $z \sim 1.6$ sample. In Figure 12, we plot the metallicity as a function, μ_α, for galaxies shown in Figure 9. Because of the small sample size, we find that the derived value of α is dependent on the number of bins. We conclude that for our sample of galaxies at $z \sim 1.6$, the scatter is minimized for $\alpha \sim 0.4$–0.5.

We find that for local galaxies, $\alpha = 0.30$ minimizes the scatter in metallicities when they are measured using the $N2$ ratio. This same value is independently derived by Andrews & Martini (2013). In Figure 13, we plot the metallicities of local (gray curve) and $z \sim 1.6$ (black curve) galaxies as a function of the μ_α that minimizes the scatter in the local relation.

Our data do not support a relation between stellar mass, metallicity, and an SFR that is independent of redshift, i.e., the FMR of Mannucci et al. (2010). When the metallicities of galaxies at $z \sim 1.6$ are plotted against the μ_α that minimizes the scatter in the local relation, a single relation is not observed (Figure 13). *The data support significant evolution in the relation between stellar mass, metallicity, and SFR. We emphasize that this is largely due to the use of aperture-corrected SFRs for local galaxies.*

7.4. The Stellar Mass, Metallicity, SFR, and Dust

Understanding the distribution of dust as a function of cosmic time and galaxy properties is critical. Several recent studies have focused on the dust properties of local galaxies (e.g., Garn & Best 2010; Xiao et al. 2012; Zahid et al. 2013c). Garn & Best (2010) derive a relation between dust extinction and stellar mass. On average, the magnitude of extinction, $A_{H\alpha}$, varies between zero and two for galaxies in the SDSS. Garn & Best (2010) perform a principal component analysis of dust extinction, stellar mass, metallicity, and SFR. From PCA, they conclude that the dominant physical property related to dust extinction in galaxies is stellar mass. The secondary correlations between dust extinction, metallicity, and SFR are primarily due to the correlation of all three of these properties to stellar mass. At a fixed stellar mass, dust extinction and metallicity are correlated in our sample of galaxies at $z \sim 1.6$ (see Figure 10). However, we note that this relation is significantly weaker than the relation between stellar mass and dust extinction. The straightforward interpretation is that galaxies increase their dust content as they build their stellar mass.

We examine the relation between dust extinction, stellar mass, metallicity, and SFR for our sample at $z \sim 1.6$ with the local relation. In Figure 14, we plot the dust extinction as a function of (A) metallicity, (B) SFR, and (C) stellar mass. The black points are the $z \sim 1.6$ sample sorted into 10 bins of stellar mass and the gray squares are the local sample sorted into 50 bins of stellar mass. Figures 14(A) and (B) clearly demonstrate that dust extinction as a function of metallicity and SFR, respectively, are significantly offset from the local relation. In contrast, the relation between dust extinction and stellar mass is similar for local galaxies and $z \sim 1.6$ galaxies (see also Paper I).

The primary difference in the relation between stellar mass and dust extinction at $z \sim 1.6$ as compared to the local universe is at the high mass end. At $z \sim 1.6$, massive galaxies exhibit larger extinction as compared to local galaxies. This may be due to the distribution of dust within galaxies or to a greater dust content in galaxies at $z \sim 1.6$. Wild et al. (2011) show that the line-to-continuum extinction is greater for galaxies with higher
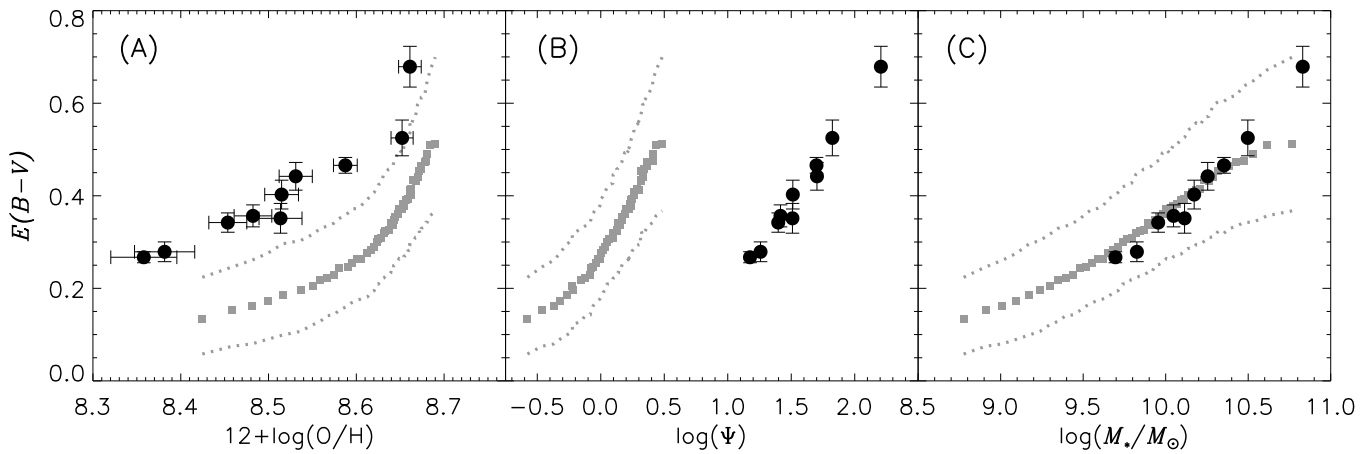
Figure 14. Relation between $E(B - V)$ and (A) metallicity, (B) SFR, and (C) stellar mass. The black points are galaxies at $z \sim 1.6$, and the gray squares are the median values of $E(B - V)$ in 50 bins of stellar mass. The dotted line denotes the interval containing the central 68% of the distribution of local galaxies.

stellar mass surface densities. They interpret this as an effect related to the dust distribution around young stars. In contrast, if the dust content is greater, this may be related to the higher SFRs of galaxies at $z \sim 1.6$. Zahid et al. (2013b) suggest that dust efflux by outflows may explain the distribution of dust in local star-forming galaxies. In this scenario, dust is slowly effluxed from galaxies by the continuous interaction of dust with the radiation field generated by ongoing star formation. The timescale of dust efflux is significantly longer than the timescale of dust production and therefore galaxies accumulate dust. The dust content of galaxies in this scenario is a balance between dust production and dust efflux. A generic prediction of this model is that massive galaxies that form stars more rapidly also have greater dust content. This is because, on average, they form their stars over a shorter period of time and do not have as much time to efflux dust from their ISM.

8. SUMMARY AND CONCLUSIONS

We derive the MZ relation using spectroscopic observations of ~160 galaxies at $z \sim 1.6$. These galaxies are observed as part of our ongoing survey of star-forming galaxies in the redshift desert. These data constitute the largest high-resolution spectroscopic sample of star-forming galaxies at $z > 1.4$ for which we can measure SFRs and metallicities from optical emission lines. The following are the main results and conclusions of our analysis.

1. There is a strong relation observed between stellar mass and metallicity for star-forming galaxies at $z \sim 1.6$. The shape of the MZ relation evolves with redshift and is steeper at early times. The most massive galaxies ($M_* \sim 10^{11} M_\odot$) in our sample at $z \sim 1.6$ have enriched to the level observed in the local universe. Less massive galaxies ($M_* \sim 10^{9.5} M_\odot$) have metallicities that are >0.25 dex lower at $z \sim 1.6$ as compared to the local universe.
2. The data support our previous results showing that the evolution of the shape in the MZ relation is a consequence of galaxies enriching to an empirical upper metallicity limit. The stellar mass where galaxies enrich to this upper metallicity limit is ~1.2 dex larger at $z \sim 1.6$ than in the local universe. Our analysis suggests that the upper metallicity limit does not evolve significantly since $z \sim 1.6$.
3. At a fixed stellar mass, metallicity is *anti*-correlated to the SFR such that, on average, galaxies with higher SFRs tend

to have lower metallicities. Similar trends are observed in the local universe.
4. Our data do not support a relation between stellar mass, metallicity, and an SFR that is independent of redshift (i.e., Mannucci et al. 2010). We observe significant evolution in the relation between stellar mass, metallicity, and SFR when comparing the local data with our $z \sim 1.6$ sample.
5. We find that at a fixed stellar mass, dustier galaxies tend to have higher metallicities. We examine the relation between dust extinction and stellar mass, metallicity, and SFR for galaxies at $z \sim 1.6$. By comparing these relations with the same relations for local galaxies, we conclude that stellar mass is closely related to the dust content of galaxies.

A consistent picture for the chemical evolution of star-forming galaxies since $z \sim 2$ is emerging. Our analysis and conclusions are based on averaging spectra from many galaxies. Measurements of metallicities in mass-selected individual galaxy samples using multiple diagnostics will be useful for assessing systematic issues. Deeper near-infrared spectroscopic surveys with greater wavelength coverage should allow us to do this soon.

REFERENCES

Aihara, H., Allende Prieto, C., An, D., et al. 2011, ApJS, 193, 29
Andrews, B. H., & Martini, P. 2013, ApJ, 765, 140
Asari, N. V., Cid Fernandes, R., Stasińska, G., et al. 2007, MNRAS, 381, 263

Baldwin, J. A., Phillips, M. M., & Terlevich, R. 1981, PASP, 93, 5
Bell, E. F., McIntosh, D. H., Katz, N., & Weinberg, M. D. 2003, ApJS, 149, 289
Berg, D. A., Skillman, E. D., Marble, A. R., et al. 2012, ApJ, 754, 98
Boissier, S., Boselli, A., Buat, V., Donas, J., & Milliard, B. 2004, A&A, 424, 465
Bordoloi, R., Lilly, S. J., Knobel, C., et al. 2011, ApJ, 743, 10
Brinchmann, J., Charlot, S., White, S. D. M., et al. 2004, MNRAS, 351, 1151
Brooks, A. M., Governato, F., Booth, C. M., et al. 2007, ApJL, 655, L17
Bruzual, G., & Charlot, S. 2003, MNRAS, 344, 1000
Calzetti, D., Armus, L., Bohlin, R. C., et al. 2000, ApJ, 533, 682
Capak, P., Aussel, H., Ajiki, M., et al. 2007, ApJS, 172, 99
Chabrier, G. 2003, PASP, 115, 763
Conroy, C., Graves, G., & van Dokkum, P. 2014, ApJ, 780, 33
Conroy, C., Gunn, J. E., & White, M. 2009, ApJ, 699, 486
Cowie, L. L., Songaila, A., Hu, E. M., & Cohen, J. G. 1996, AJ, 112, 839
Cullen, F., Cirasuolo, M., McLure, R. J., Dunlop, J. S., & Bowler, R. A. A. 2014, MNRAS, 440, 2300
Daddi, E., Cimatti, A., Renzini, A., et al. 2004, ApJ, 617, 746
Daddi, E., Dickinson, M., Morrison, G., et al. 2007, ApJ, 670, 156
Davé, R., Finlator, K., & Oppenheimer, B. D. 2011, MNRAS, 416, 1354
Denicoló, G., Terlevich, R., & Terlevich, E. 2002, MNRAS, 330, 69
Ellison, S. L., Patton, D. R., Simard, L., & McConnachie, A. W. 2008, ApJL, 672, L107
Erb, D. K., Shapley, A. E., Pettini, M., et al. 2006, ApJ, 644, 813
Finlator, K., & Davé, R. 2008, MNRAS, 385, 2181
Fontana, A., Pozzetti, L., Donnarumma, I., et al. 2004, A&A, 424, 23
Foster, C., Hopkins, A. M., Gunawardhana, M., et al. 2012, A&A, 547, A79
Gallazzi, A., Charlot, S., Brinchmann, J., White, S. D. M., & Tremonti, C. A. 2005, MNRAS, 362, 41
Garn, T., & Best, P. N. 2010, MNRAS, 409, 421
Geller, M. J., Hwang, H. S., Fabricant, D. G., et al. 2014, arXiv:1405.7704
Groves, B., Brinchmann, J., & Walcher, C. J. 2012, MNRAS, 419, 1402
Hainline, K. N., Shapley, A. E., Kornei, K. A., et al. 2009, ApJ, 701, 52
Heckman, T. M., Robert, C., Leitherer, C., Garnett, D. R., & van der Rydt, F. 1998, ApJ, 503, 646
Henry, A., Scarlata, C., Domínguez, A., et al. 2013, ApJL, 776, L27
Hopkins, A. M., & Beacom, J. F. 2006, ApJ, 651, 142
Hummer, D. G., & Storey, P. J. 1987, MNRAS, 224, 801
Ilbert, O., Capak, P., Salvato, M., et al. 2009, ApJ, 690, 1236
Iwamuro, F., Moritani, Y., Yabe, K., et al. 2012, PASJ, 64, 59
Iwamuro, F., Motohara, K., Maihara, T., Hata, R., & Harashima, T. 2001, PASJ, 53, 355
Kashino, D., Silverman, J. D., Rodighiero, G., et al. 2013, ApJL, 777, L8
Kauffmann, G., Heckman, T. M., Tremonti, C., et al. 2003, MNRAS, 346, 1055
Kennicutt, R. C., Jr. 1998, ARA&A, 36, 189
Kewley, L. J., & Dopita, M. A. 2002, ApJS, 142, 35
Kewley, L. J., Dopita, M. A., Leitherer, C., et al. 2013a, ApJ, 774, 100
Kewley, L. J., & Ellison, S. L. 2008, ApJ, 681, 1183
Kewley, L. J., Groves, B., Kauffmann, G., & Heckman, T. 2006, MNRAS, 372, 961
Kewley, L. J., Jansen, R. A., & Geller, M. J. 2005, PASP, 117, 227
Kewley, L. J., Maier, C., Yabe, K., et al. 2013b, ApJL, 774, L10
Kimura, M., Maihara, T., Iwamuro, F., et al. 2010, PASJ, 62, 1135
Kirby, E. N., Martin, C. L., & Finlator, K. 2011, ApJL, 742, L25
Kobulnicky, H. A., & Kewley, L. J. 2004, ApJ, 617, 240
Kulas, K. R., Mclean, I. S., Shapley, A. E., et al. 2013, ApJ, 774, 130
Lara-López, M. A., Cepa, J., Bongiovanni, A., et al. 2010, A&A, 521, L53
Larson, R. B. 1974, MNRAS, 169, 229
Laskar, T., Berger, E., & Chary, R.-R. 2011, ApJ, 739, 1
Lee, H., Skillman, E. D., Cannon, J. M., et al. 2006, ApJ, 647, 970

Lequeux, J., Peimbert, M., Rayo, J. F., Serrano, A., & Torres-Peimbert, S. 1979, A&A, 80, 155
Lilly, S. J., Carollo, C. M., Pipino, A., Renzini, A., & Peng, Y. 2013, ApJ, 772, 119
Lilly, S. J., Le Févre, O., Renzini, A., et al. 2007, ApJS, 172, 70
Maier, C., Lilly, S. J., Carollo, C. M., et al. 2006, ApJ, 639, 858
Maier, C., Lilly, S. J., Carollo, C. M., Stockton, A., & Brodwin, M. 2005, ApJ, 634, 849
Maiolino, R., Nagao, T., Grazian, A., et al. 2008, A&A, 488, 463
Mannucci, F., Cresci, G., Maiolino, R., Marconi, A., & Gnerucci, A. 2010, MNRAS, 408, 2115
Mannucci, F., Cresci, G., Maiolino, R., et al. 2009, MNRAS, 398, 1915
Marino, R. A., Rosales-Ortega, F. F., Sánchez, S. F., et al. 2013, A&A, 559, A114
Markwardt, C. B. 2009, in ASP Conf. Ser. 411, Astronomical Data Analysis Software and Systems XVIII, ed. D. A. Bohlender, D. Durand, & P. Dowler (San Francisco, CA: ASP), 251
Martin, C. L., Kobulnicky, H. A., & Heckman, T. M. 2002, ApJ, 574, 663
Mathews, W. G., & Baker, J. C. 1971, ApJ, 170, 241
McCracken, H. J., Capak, P., Salvato, M., et al. 2010, ApJ, 708, 202
Moustakas, J., Zaritsky, D., Brown, M., et al. 2011, arXiv:1112.3300
Nagao, T., Maiolino, R., & Marconi, A. 2006, A&A, 459, 85
Newman, S. F., Genzel, R., Förster-Schreiber, N. M., et al. 2012, ApJ, 761, 43
Niino, Y. 2012, ApJ, 761, 126
Padmanabhan, N., et al. 2008, ApJ, 674, 1217
Panter, B., Jimenez, R., Heavens, A. F., & Charlot, S. 2008, MNRAS, 391, 1117
Peng, Y.-j., Lilly, S. J., Kovač, K., et al. 2010, ApJ, 721, 193
Pérez-Montero, E., Contini, T., Lamareille, F., et al. 2013, A&A, 549, A25
Pettini, M., & Pagel, B. E. J. 2004, MNRAS, 348, L59
Reddy, N. A., Erb, D. K., Pettini, M., Steidel, C. C., & Shapley, A. E. 2010, ApJ, 712, 1070
Renzini, A. 1997, ApJ, 488, 35
Rigby, J. R., Wuyts, E., Gladders, M. D., Sharon, K., & Becker, G. D. 2011, ApJ, 732, 59
Salim, S., Rich, R. M., Charlot, S., et al. 2007, ApJS, 173, 267
Salpeter, E. E. 1955, ApJ, 121, 161
Sánchez, S. F., Rosales-Ortega, F. F., Jungwiert, B., et al. 2013, A&A, 554, A58
Savaglio, S., Glazebrook, K., Le Borgne, D., et al. 2005, ApJ, 635, 260
Scoville, N., Aussel, H., Brusa, M., et al. 2007, ApJS, 172, 1
Stott, J. P., Sobral, D., Bower, R., et al. 2013, MNRAS, 436, 1130
Stoughton, C., Lupton, R. H., Bernardi, M., et al. 2002, AJ, 123, 485
Strauss, M. A., Weinberg, D. H., Lupton, R. H., et al. 2002, AJ, 124, 1810
Thomas, D., Maraston, C., Bender, R., & Mendes de Oliveira, C. 2005, ApJ, 621, 673
Thomas, D., Steele, O., Maraston, C., et al. 2013, MNRAS, 431, 1383
Torrey, P., Vogelsberger, M., Genel, S., et al. 2013, MNRAS, 438, 1985
Tremonti, C. A., Heckman, T. M., Kauffmann, G., et al. 2004, ApJ, 613, 898
Wild, V., Charlot, S., Brinchmann, J., et al. 2011, MNRAS, 417, 1760
Wuyts, E., Kurk, J., Förster Schreiber, N. M., et al. 2014, ApJL, 789, L40
Xiao, T., Wang, T., Wang, H., et al. 2012, MNRAS, 421, 486
Yabe, K., Ohta, K., Iwamuro, F., et al. 2012, PASJ, 64, 60
Yates, R. M., Kauffmann, G., & Guo, Q. 2012, MNRAS, 422, 215
Yuan, T.-T., Kewley, L. J., & Richard, J. 2013, ApJ, 763, 9
Zahid, H. J., Bresolin, F., Kewley, L. J., Coil, A. L., & Davé, R. 2012a, ApJ, 750, 120
Zahid, H. J., Dima, G. I., Kewley, L. J., Erb, D. K., & Davé, R. 2012b, ApJ, 757, 54
Zahid, H. J., Geller, M. J., Kewley, L. J., et al. 2013a, ApJL, 771, L19
Zahid, H. J., Kewley, L. J., & Bresolin, F. 2011, ApJ, 730, 137
Zahid, H. J., Torrey, P., Kudritzki, R., et al. 2013b, MNRAS, 436, 1852
Zahid, H. J., Torrey, P., Vogelsberger, M., et al. 2014, Ap&SS, 349, 873
Zahid, H. J., Yates, R. M., Kewley, L. J., & Kudritzki, R. P. 2013c, ApJ, 763, 92